Short-lived alkaline magmatism related to the Réunion plume in the Deccan Large Igneous Province: inferences from petrology, $^{40}Ar/^{39}Ar$ geochronology and palaeomagnetism of lamprophyre from the Sarnu-Dandali Alkaline Igneous Complex

Ashish Dongre[1]*, P. S. Dhote[2], P. Zamarkar[1], S. J. Sangode[1], G. Belyanin[3], D. C. Meshram[1], S. K. Patil[4], Aaheri Karmakar[5] and Lokant Jain[1]

[1]Department of Geology, Savitribai Phule Pune University, Pune 411007, India

[2]Kuwait Oil Company, PO Box 9758, Ahmadi 61008, Kuwait

[3]Department of Geology, University of Johannesburg, Auckland Park 2006, South Africa

[4]Dr. K.S.K. Geomagnetic Research Laboratory, Allahabad 221505, India

[5]Department of Geology, Banaras Hindu University, Varanasi 221005, India

AD, 0000-0002-0216-9753; PSD, 0000-0001-8434-6225; LJ, 0000-0001-5103-5711

*Correspondence: andongare@unipune.ac.in; andongrey@gmail.com

Abstract: Available geochronological information on Deccan indicates prolonged (started at 68.5 Ma) alkaline magmatism related to the Réunion mantle plume based on the $^{40}Ar/^{39}Ar$ ages from Sarnu-Dandali and Mundwara alkaline complexes. We studied in detail an alkaline lamprophyre, from the Sarnu-Dandali Complex, rich in groundmass (magmatic) as well as xenocrystic phlogopites and clinopyroxenes. $^{40}Ar/^{39}Ar$ age determinations of the phlogopites from this lamprophyre reveal two distinct ages of 65.44 $\pm$ 1.5 Ma and 68.17 $\pm$ 1 Ma. However, palaeomagnetic results show a VGP at 32.31° N and 298.52° E concordant with that of the Deccan Super Pole at 65.5 Ma and support the younger eruption age at *c.* 65.44 $\pm$ 1.5 Ma. Analysed phlogopites lack any signs of retention of excess radiogenic Ar and yield similar inverse isochron ages, which suggests that the older age of *c.* 68.17 $\pm$ 1 Ma belongs to the crystallization of xenocrystic phlogopite during mantle metasomatism. Trace element compositions support derivation of lamprophyre magma from an OIB-type enriched (metasomatized) mantle source with an involvement of phlogopite.

This finding suggests that the pre-Deccan ages of *c.* 68–69 Ma reported previously may reflect the timing of metasomatism of the subcratonic lithospheric mantle during the separation of Greater-Seychelles from India at *c.* 68.5 Ma. The absence of pre-Deccan alkaline rocks therefore indicates the short duration (between 67–65 Ma) of alkaline as well as small-volume, volatile-rich magmatism directly related to the Réunion (Deccan) plume.

Supplementary material: Figure 1 – Field photographs of lamprophyre dyke; Figure 2 – Clinopyroxene compositions; Figure 3 – $^{40}Ar/^{39}Ar$ plateau spectra; Table 1 – Ar-Ar analytical data; Table 2 – Compilation of Ar-Ar and U-Pb ages for Deccan alkaline rocks are available at https://doi.org/10.6084/m9.figshare.c.5490881

Flood basalt eruptions in continental large igneous provinces (LIPs) are usually associated with the alkaline magmatism (Sun *et al.* 2014). In the case of the Deccan flood basalt volcanism, alkaline rocks are considered to pre-date (erupted during Maastrichtian, 72–66 Ma) and post-date (erupted during Danian, 66-61.6 Ma), as well as be synchronous with the eruption of the bulk of tholeiite magmatism during 66.4 to 65.4 Ma (Renne *et al.* 2015; Schoene *et al.* 2015; Parisio *et al.* 2016; Sprain *et al.* 2019). A broad spectrum of alkaline rocks that are temporally and spatially related to the Deccan LIP comprises alkali basalt and gabbro, lamprophyre (alkaline), carbonatite, nepheline syenite, phonolite, trachyte and mela-nephelinite. Prominent alkaline complexes associated with the Deccan LIP, where such rocks have been known are Chhota Udepur, Girnar, Murud-Janjira, Mundwara and Sarnu-Dandali, and these complexes are mostly located on the periphery of the present extent of the Deccan Traps (Fig. 1). The tholeiites of Deccan LIP have been extensively studied for their morphology, geochemistry and geochronology (see Kale *et al.* 2019 and references therein) as compared to the associated small-volume, mafic-ultramafic, volatile-rich alkaline rocks.

Réunion plume related magmatism older than the voluminous Deccan Trap tholeiites (i.e. earlier than

From: Krmíček, L. and Chalapathi Rao, N. V. (eds) 2022. *Lamprophyres, Lamproites and Related Rocks: Tracers to Supercontinent Cycles and Metallogenesis*. Geological Society, London, Special Publications, **513**, 381–411.
First published online August 23, 2021, https://doi.org/10.1144/SP513-2021-34

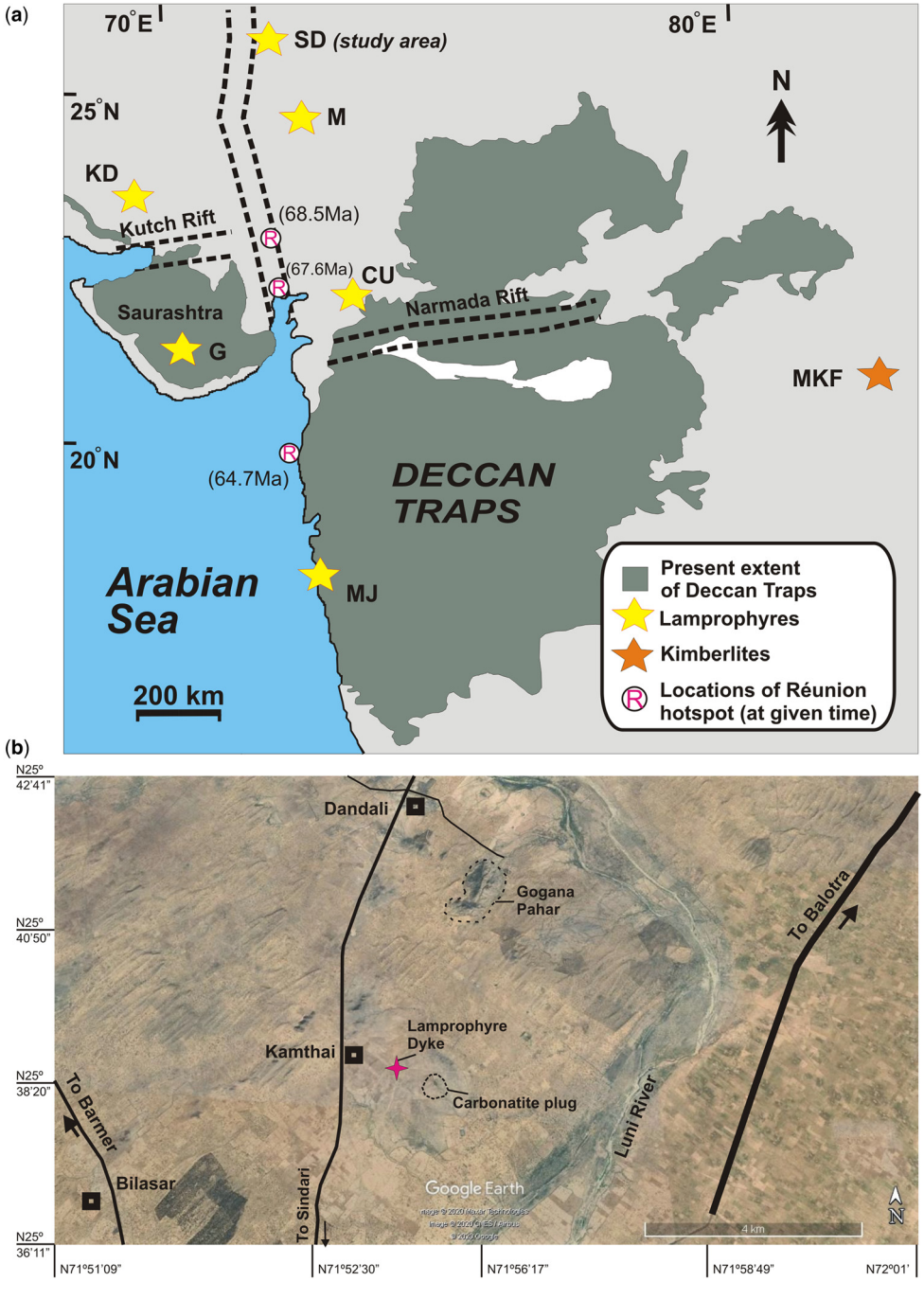

Fig. 1. (**a**) Geological map of the part of Indian subcontinent showing the present extent of Deccan Traps (modified after Dongre *et al.* 2017). Prominent locations of lamprophyres, and Deccan related Group 2 kimberlites are shown, which mostly occur near the rifts and at the peripheral parts of the present extent of Deccan Traps. Abbreviations: SD, Sarnu-Dandali; M, Mundwara; KD, Kaladongar; G, Girnar; CU, Chhota Udepur; MJ, Murud Janjira; MKF, Mainpur Kimberlite Field. Tentative locations of the Réunion hotspot at a given time are from Bhattacharya and Yatheesh (2015). (**b**) Google Earth image of the Sarnu-Dandali area showing location of the lamprophyre dyke (modified after Sheth *et al.* 2017).

66.4 Ma) is referred to here as pre-Deccan. Such pre-Deccan rocks are typically known from the alkaline complexes in the northwestern parts of the Indian subcontinent and prominent among them are Mundwara and Sarnu-Dandali, which are at more than 500 km distance from the main Deccan flood basalt exposures in western-central India (Basu *et al.* 1993; Sen *et al.* 2012) (Fig. 1). Based on the $^{40}Ar/^{39}Ar$ ages from these two alkaline complexes, it has been considered that the Deccan volcanism began at *c.* 68.5 Ma and continued over an extended duration (e.g. Basu *et al.* 1993; Pande 2002; Chenet *et al.* 2007; Parisio *et al.* 2016). The presence of pre-Deccan ages further indicates that the magmatism related to the Réunion hotspot on the Indian subcontinent initiated as small-volume, alkaline rock eruptions at *c.* 2 million years before the rapid extrusion of voluminous tholeiites and supported a time-related southward migration of volcanism on the Indian subcontinent.

Basu *et al.* (1993) analysed three biotite grains from alkali pyroxenite rock from the Sarnu-Dandali area, which gave well-defined $^{40}Ar/^{39}Ar$ apparent age plateaus with a weighted mean of 68.57 $\pm$ 0.08 Ma. The presence of alkali pyroxenite rocks in the Sarnu-Dandali Alkaline Complex, as irregular patches in the syenites and as small intrusions, have been known since the early 1990s (Chandrasekaran *et al.* 1990). However, pyroxenite intrusions showing characteristic cumulate texture and containing biotite as phenocrystic phases do not occur in the Sarnu-Dandali area during the present work as well as during other previous extensive field investigations (e.g. Bhushan 2015; Dhote 2015; Vijayan *et al.* 2016). Older pre-Deccan rocks related to the Réunion hotspot in the Sarnu-Dandali Alkaline Complex were not recognized in the recent geochronological studies as well (e.g. Sheth *et al.* 2017). Precise identification of rock/magmatic type, its composition (mineralogical and geochemical) and accurate eruption age is, therefore, significant to better understand the evolution of the province, relative timings of alkaline and small-volume mafic-ultramafic magmatism, and time-related migration of volcanism in the Deccan LIP.

In this communication, we report a detailed study of a lamprophyre intrusion, which is notably rich in phlogopites and clinopyroxenes, from the Sarnu-Dandali Complex. Our integrated study on mineralogy, $^{40}Ar/^{39}Ar$ geochronology and palaeomagnetism confirms the presence of younger, Deccan synchronous (*c.* 66 Ma) alkaline rocks in the Sarnu-Dandali and non-existence of pre-Deccan magmatism as reported previously. We further show that the pre-Deccan ages of *c.* 68–69 Ma obtained in the Sarnu-Dandali indeed reflect the timing of metasomatism of the subcratonic lithospheric mantle induced during the separation of Seychelles-Laxmi Ridge from India.

Geological setting of the Sarnu-Dandali Complex

Sarnu-Dandali Alkaline Igneous Complex in the northwestern part of the Indian subcontinent is considered to be a pre-Deccan magmatic province. It is located in the eastern part of the Barmer Basin, which was developed in a rhyolite-granite basement of *c.* 750 Ma Malani volcanics. Malani rhyolites and Sarnu sandstone (Early Cretaceous age) combinedly form the basement of the Sarnu-Dandali Complex that hosts different alkaline rocks.

The complex consists mostly of subvolcanic plutons of the alkali syenite that are intruded by the dykes as well as lava flows of the mafic and felsic alkaline rocks. The mafic alkaline rocks in the area include nephelinites, mela-nephelinites, ijolites and carbonatites. Alkaline, small-volume carbonatite magmatism in the form of veins, dykes and small plugs, intruding syenites, have been reported from the Sarnu-Dandali area and hosts a world-class deposit of rare earth elements (REEs) having resources of 4.91 million tons (Bhushan and Kumar 2013). The area also contains Mesozoic sedimentary rocks having potential hydrocarbon reserves (Dolson *et al.* 2015). A basalt flow underlying the Early Cretaceous Sarnu sandstone in the Sarnu hills was recently reported from this area (Bladon *et al.* 2015).

Recent geochronological investigations obtained 88–86 Ma ages on the basement rocks of syenites, nephelinites, phonolites and rhyolites (Sheth *et al.* 2017). Sheth *et al.* (2017) recognized the Deccan age (*c.* 66 Ma) mela-nephelinite flow in the area as well and showed polychronous emplacement of alkaline rocks in the complex. For details and recent work on the geology of the Sarnu-Dandali Complex, one can refer to Vijayan *et al.* (2016) and Sheth *et al.* (2017). Narsimhan *et al.* (2019) studied the palaeomagnetism of the alkaline rocks from the Sarnu-Dandali and Mundwara complexes and suggested coeval emplacement of alkaline rocks with Deccan eruptions.

The lamprophyre dyke studied here was reported recently by the Geological Survey of India from the north of the Kamthai area (Dhote 2015). The N15° W trending lamprophyre dyke (N 25° 38′ 09″ and E 71° 55′ 36″) intrudes the alkali syenites. The dyke is typically 2–3 metres wide having exposures of about 100 metres in length and mostly covered by desert sand in the area (Supplementary Fig. 1a).

Material and methods

A CAMECA SX-Five electron probe micro-analyser (EPMA) with LaB_6 electron gun source, installed at the Banaras Hindu University, Varanasi, was used

for quantitative mineral analyses. Wavelength dispersive spectrometry (WDS) with TAP, PET and LIF crystals were deployed. Instrument settings used for analyses were: acceleration voltage of 15 kV, a beam current of 10 nA, and a beam diameter of 1 μm. Uncertainty on the major element analyses was <1% and for trace elements varied between 3 and 5%. The instrument was calibrated using a number of natural and synthetic standards as detailed by Pandey *et al.* (2018*a*).

Five representative rock samples collected from the lamprophyre dyke were crushed and powdered using an agate mill. Bulk rock compositions were analysed at Bureau Veritas, Canada. Major element concentrations were determined by the inductively coupled plasma-optical emission spectrometry (ICP-OES) technique (SpectroCiros- CCD) and trace elements and REE were analysed by inductively coupled plasma-mass spectrometry (ICP-MS) using a Perkin Elmer Sciex Elan 9000 system, following lithium metaborate/tetraborate fusion of the sample powder. The calibration of the instrument was accomplished using reference samples and internal standards, while the accuracy and precision of the data were checked through the use of certified in-house reference standards like SO-19, GS-311 and GS-910.

For the $^{40}Ar/^{39}Ar$ analyses, all the megascopically visible large size grains (xenocrysts) of phlogopites were removed from sample selection before analysis. Phlogopite phenocrysts were separated and handpicked from the coarsely crushed samples using a stereo zoom microscope. Phlogopite grains were repeatedly cleaned ultrasonically in distilled water, and *c.* 6 mg per irradiation were subsequently wrapped in light aluminum foil. They were subsequently vacuum-sealed in a silica glass tube of 8 mm inner diameter as part of a 50 mm-long stack and irradiated at the NTP radioisotopes SAFARI1 nuclear reactor at Pelindaba, South Africa, in position B2W (not cadmium-shielded) with the reactor running at 20 MW. The samples were subjected to 5 hours irradiation and subsequently analysed at the central analytical facility (Spectrum) of the University of Johannesburg by stepwise heating, using a defocused beam from a continuous Nd-YAG 1064 nm laser. Heating for each step lasted 5 min. Although the step temperatures could not be measured, we ensured that the process started at a temperature well below visible luminosity, probably at *c.* 400°C, following Conrad *et al.* (2011). The final steps yielded a bright yellow glow, probably at *c.* 1300°C. Ar isotope ratios were measured on a MAP 215-50 mass spectrometer equipped with Johnston focused-flow electron multiplier used in analogue mode. Aliquots of the McClure Mountain amphibole (523.1 ± 2.6 Ma) (Renne *et al.* 1998) standard, placed at different levels in the sample stack, were used as monitors. The value for the ^{40}K decay constant $(5.554 \pm 0.014) \times 10^{-10}$ yr^{-1} derived by Kossert and Günther (2004) and Renne *et al.* (2010) was utilized. Blank measurements were done after every third or fourth step run. Measurement control and data reduction were carried out using an in-house software suite that includes full error propagation by Monte Carlo procedures. Age uncertainties are shown at the 95% (2σ) confidence level.

Palaeomagnetic sampling was carried out using routine methods and by avoiding the weathered or fractured locations to get compact samples from exposed parts of the dyke. Over 17 samples were collected, and finally, after removal of surface specimens from each core, a total of 40 specimens were obtained for the detailed demagnetization analysis. The thermal demagnetization was conducted in 13 steps of 100, 200, 250, 300, 350, 400, 450, 500, 530, 560, 580, 600 and the AF demagnetization was imparted using the fields of 10, 15, 20, 25, 30, 35, 40, 45, 50, 60, 70 and 80 mT. The remanences were measured using AGICO JR6A at KSKRL Geomagnetic laboratory, Indian Institute of Geomagnetism, Allahabad (India). The data were inferred using vector migration plots and other routine statistics in Remasoft 3.0 version of the AGICO palaeomagnetic analysis software. The principal component analysis (PCA) means, scatter and angular deviations were calculated independently at specimen level for the demagnetization data.

Results

Petrography

The studied Sarnu-Dandali lamprophyre (SDL) is dark grey to black, mesocratic, shows fine-grained nature and typical porphyritic and panidiomorphic textures. The groundmass is largely composed of mica, clinopyroxene, alkali feldspar, nepheline, spinels and sphene. Clinopyroxenes occur as prominent euhedral, six-sided phenocrysts as well as large xenocrysts (Figs 2 & 3). Few small-sized, discrete grains of aegirine are also present in the groundmass. Varied-sized phlogopite grains are present throughout the dyke where large-sized fragments show signs of deformation and appear to be a disintegrated part of the xenocrystic suite (Fig. 2). Clusters of large-sized xenocrysts are easily visible megascopically (Fig. 2a). Subhedral, fine flakes of phlogopite are also abundant in the lamprophyre groundmass. All the constituent minerals of the dyke are fresh and devoid of significant alteration. SDL shows the abundant presence of crustal and mantle xenoliths. A peridotite xenolith comprising noticeable phlogopite grains is also identified in the present study

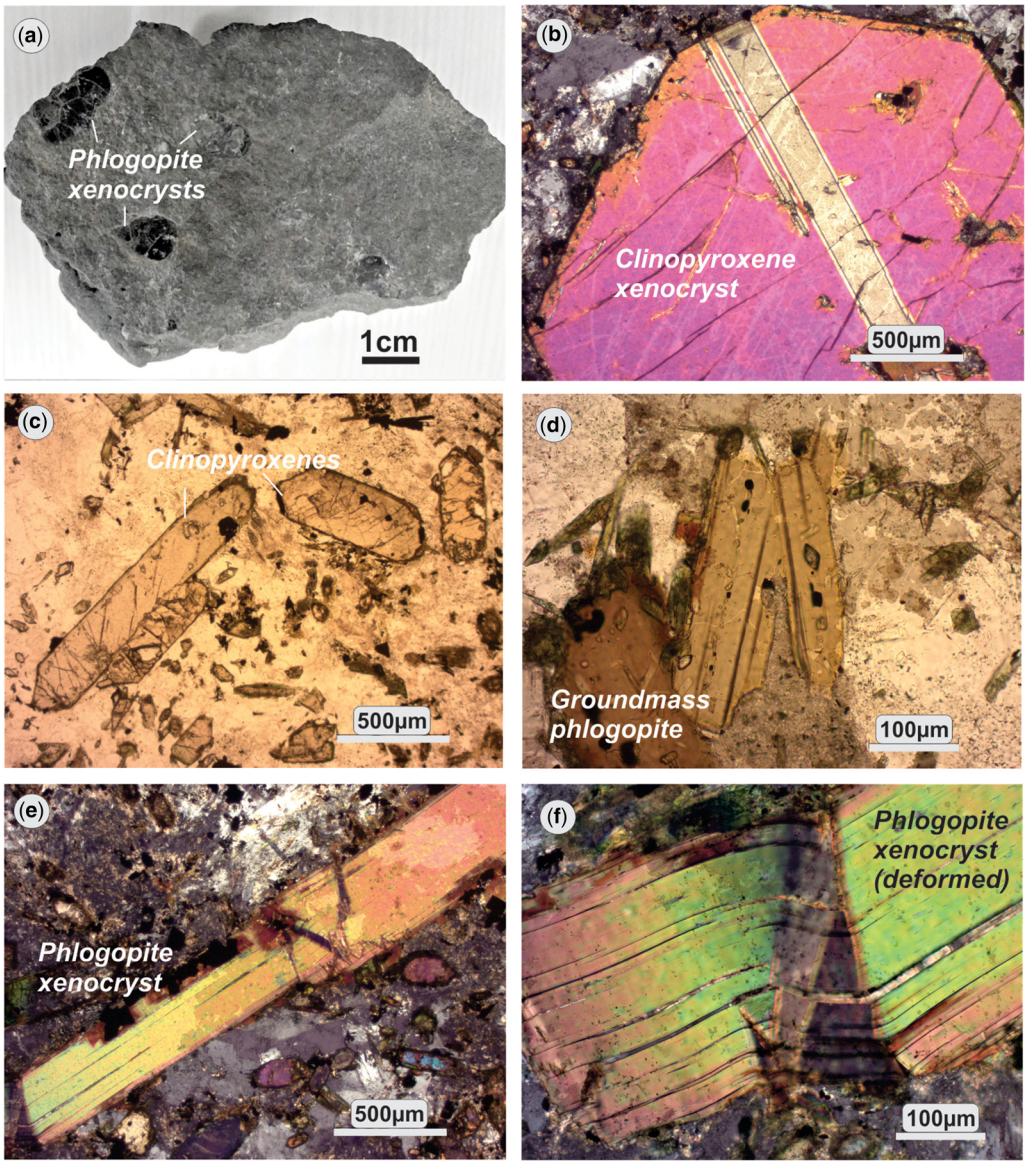

Fig. 2. (**a**) Image showing sample of lamprophyre dyke and its megascopic features, abundant xenocrysts of phlogopites can be seen. Photomicrographs showing (**b**) euhedral clinopyroxene xenocryst, (**c**) lamprophyre groundmass rich in euhedral phenocrysts of clinopyroxenes imparting panidiomorphic texture, (**d**) magmatic phlogopite crystals in the groundmass, (**e**) part of elongated subhedral xenocryst of phlogopite, (**f**) part of a deformed and broken phlogopite xenocryst in the lamprophyre groundmass.

(Supplementary Fig. 1b). Representative compositions of constituent minerals are provided in Table 1.

Mineral compositions

Clinopyroxene. Phenocrysts (*c*. 500 μ in size, Fig. 2) and smaller grains of clinopyroxene are abundant in the groundmass of the SDL dyke. Few xenocrysts having a size larger than 500 μ (Fig. 2b) are also captured by the SDL magma. Clinopyroxenes mostly show six-sided, euhedral shapes and at a few places, twinned crystals are also evident (Fig. 2b, c). Dominant clinopyroxenes are typically diopsides having composition $Wo_{47\text{-}60}En_{23\text{-}41}Fs_{8\text{-}9}$. Clinopyroxene

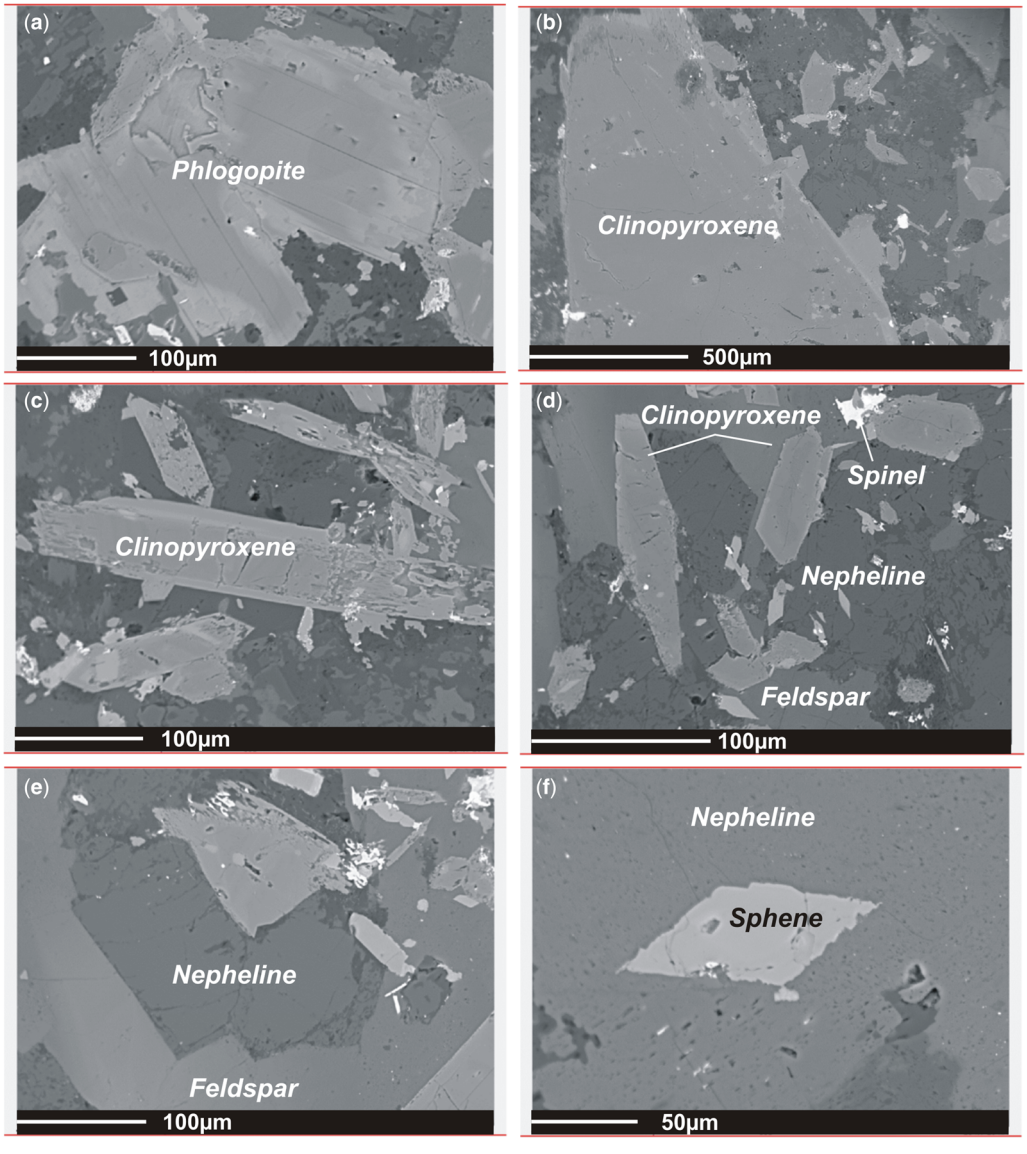

Fig. 3. Back-scattered electron (BSE) images showing (**a**) microphenocrysts of phlogopites that are unaltered and without any zoning and inclusions set in the lamprophyre groundmass, (**b**) euhedral-shaped clinopyroxenes, (**c**) aegirine occurring as discrete grain in the groundmass, (**d**) groundmass of the lamprophyre rich in clinopyroxene, nepheline, feldspar and spinel, (**e**) nepheline and feldspars in close textural relationship in the groundmass, (**f**) sphene crystal included in a nepheline in the groundmass.

from Sarnu-Dandali lamprophyre seems to be higher in Ca content as compared to other lamprophyres from the Deccan LIP (Supplementary Fig. 2). Their TiO_2 content ranges from 1.6–4.2 wt%, CaO from 21.6–25.1 wt% and Al_2O_3 from 3.3–8.1 wt%. High Ti-Al-Ca content of clinopyroxene is a characteristic of alkaline lamprophyres (Fig. 4a) and anorogenic magmatic rocks (Fig. 4b). However, clinopyroxenes from other lamprophyres from the Deccan LIP show transitional characters from orogenic to anorogenic fields as seen in Figure 4b. The compositional difference is noticed in a few clinopyroxenes, which reflects aegirine enrichment. Aegirine is present as small discrete grains in the groundmass having higher Na_2O (*c.* 12 wt%), TiO_2 (*c.* 4 wt%) and lower CaO (4 wt%).

Table 1. *Representative chemical compositions of different mineral phases from lamprophyre dyke (in wt%)*

Mineral	Clinopyroxene													
Analysis	1	2	3	4	5	6	7	8	9	10	11	12	13	14
SiO_2	44.65	46.88	45.17	47.17	48.16	45.62	44.95	46.24	43.12	44.90	48.28	43.89	44.52	50.96
TiO_2	3.10	2.32	3.53	1.76	2.22	2.90	3.62	3.06	4.15	3.46	1.96	4.18	3.82	4.73
Al_2O_3	6.84	4.70	6.79	4.38	4.15	4.84	6.99	6.16	8.05	6.83	3.27	7.17	7.09	1.29
FeO	9.14	9.03	6.90	12.30	8.32	7.36	6.49	6.05	6.92	6.83	7.96	8.71	7.46	23.51
MnO	0.27	0.29	0.02	0.51	0.22	0.18	0.07	0.06	0.13	0.06	0.31	0.11	0.20	0.88
MgO	11.07	11.24	13.06	9.90	12.40	12.57	13.13	13.91	12.21	13.00	13.17	11.64	11.95	0.67
CaO	23.35	23.01	23.64	22.47	23.41	25.13	24.16	24.07	23.97	24.25	24.00	21.65	23.68	4.34
Na_2O	0.80	1.01	0.64	1.12	0.67	0.40	0.12	0.09	0.22	0.22	0.33	0.63	0.79	12.11
Cr_2O_3	0.00	0.00	0.00	0.02	0.00	0.00	0.00	0.00	0.00	0.00	0.00	0.00	0.00	0.01
P_2O_5	0.39	0.41	0.56	0.45	0.45	0.51	0.45	0.46	0.46	0.48	0.55	0.47	0.50	0.11
Total	99.61	98.89	100.30	100.07	100.00	99.57	99.99	100.10	99.23	100.03	99.84	98.64	100.01	98.65
	Cations based on 6 oxygen atoms													
Si	1.706	1.796	1.694	1.810	1.814	1.736	1.689	1.727	1.641	1.690	1.821	1.684	1.683	2.042
Ti	0.089	0.067	0.099	0.051	0.063	0.083	0.102	0.086	0.119	0.098	0.055	0.121	0.109	0.143
Al	0.308	0.212	0.300	0.198	0.184	0.217	0.310	0.271	0.361	0.303	0.146	0.324	0.316	0.061
Fe^{2+}	0.292	0.289	0.216	0.395	0.262	0.234	0.204	0.189	0.220	0.215	0.251	0.279	0.236	0.788
Mn	0.009	0.009	0.001	0.016	0.007	0.006	0.002	0.002	0.004	0.002	0.010	0.004	0.006	0.030
Mg	0.631	0.642	0.730	0.567	0.696	0.713	0.736	0.775	0.692	0.729	0.741	0.666	0.674	0.040
Ca	0.956	0.945	0.949	0.924	0.945	1.025	0.973	0.963	0.977	0.978	0.970	0.890	0.959	0.186
Na	0.059	0.075	0.046	0.083	0.049	0.029	0.009	0.007	0.017	0.016	0.024	0.047	0.058	0.941
Cr	0.000	0.000	0.000	0.001	0.000	0.000	0.000	0.000	0.000	0.000	0.000	0.000	0.000	0.000
P	0.012	0.013	0.018	0.014	0.014	0.017	0.014	0.014	0.015	0.015	0.018	0.015	0.016	0.004
Total	4	4	4	4	4	4	4	4	4	4	4	4	4	4

(*Continued*)

Table 1. *Continued.*

Mineral	Groundmass phlogopite													
Analysis	1	2	3	4	5	6	7	8	9	10	11	12	13	14
SiO_2	34.87	34.26	35.33	34.68	34.79	34.88	34.79	34.72	34.18	34.02	37.08	35.54	34.42	36.64
TiO_2	6.04	6.10	5.99	6.08	6.05	6.02	6.16	6.15	5.56	4.67	4.27	4.72	4.65	4.84
Al_2O_3	14.56	14.92	14.74	14.79	14.78	14.38	14.57	14.88	14.37	14.83	14.59	15.34	15.42	15.32
FeO	13.38	13.46	13.52	13.08	13.39	13.05	13.25	12.84	14.64	15.52	13.95	8.79	14.03	10.05
MnO	0.32	0.19	0.24	0.19	0.15	0.19	0.26	0.17	0.36	0.18	0.21	0.17	0.25	0.04
MgO	15.55	14.81	14.83	14.94	14.63	15.14	14.91	14.65	13.95	13.57	14.14	17.97	15.11	18.14
CaO	0.00	0.03	0.01	0.01	0.01	0.02	0.02	0.01	0.04	0.11	0.13	0.13	0.13	0.10
Na_2O	0.71	0.69	0.66	0.65	0.68	0.62	0.70	0.66	0.74	0.60	0.50	0.42	0.61	0.63
K_2O	8.59	8.48	8.63	8.34	8.55	8.55	8.53	8.55	8.70	7.94	8.50	8.53	7.81	8.54
Cr_2O_3	0.00	0.00	0.00	0.00	0.01	0.00	0.00	0.01	0.00	0.00	0.34	0.01	0.00	0.06
F	0.99	0.94	1.02	0.79	0.80	0.78	0.65	0.86	1.20	0.06	0.40	0.28	0.27	0.42
Cl	0.01	0.01	0.01	0.02	0.01	0.02	0.01	0.01	0.02	0.01	0.01	0.01	0.11	0.00
BaO	0.60	1.69	1.51	1.20	1.55	1.69	1.37	1.35	0.82	1.73	0.19	1.12	2.05	0.65
Total	95.63	95.60	96.50	94.77	95.40	95.35	95.23	94.86	94.58	93.233	94.319	93.035	94.838	95.421
	Cations based on 22 oxygen atoms													
Si	5.277	5.246	5.341	5.298	5.313	5.330	5.304	5.310	5.303	5.331	5.597	5.371	5.285	5.399
Ti	0.688	0.702	0.681	0.699	0.694	0.692	0.707	0.708	0.649	0.550	0.485	0.537	0.537	0.536
Al	2.597	2.692	2.627	2.664	2.659	2.590	2.619	2.682	2.628	2.739	2.596	2.731	2.791	2.661
Fe^{2+}	1.693	1.724	1.709	1.671	1.709	1.667	1.689	1.642	1.899	2.033	1.761	1.110	1.801	1.238
Mn	0.041	0.025	0.031	0.024	0.020	0.024	0.034	0.023	0.047	0.024	0.026	0.022	0.032	0.005
Mg	3.508	3.381	3.343	3.403	3.330	3.450	3.390	3.340	3.227	3.170	3.181	4.049	3.460	3.983
Ca	0.000	0.005	0.002	0.002	0.002	0.003	0.003	0.002	0.007	0.019	0.021	0.021	0.022	0.016
Na	0.208	0.205	0.192	0.191	0.201	0.185	0.206	0.195	0.223	0.181	0.146	0.124	0.180	0.179
K	1.658	1.657	1.665	1.625	1.665	1.667	1.660	1.669	1.723	1.587	1.636	1.644	1.530	1.604
Cr	0.000	0.000	0.000	0.000	0.001	0.000	0.000	0.001	0.000	0.000	0.041	0.001	0.000	0.000
F	0.475	0.455	0.486	0.384	0.387	0.377	0.315	0.416	0.587	0.029	0.190	0.135	0.132	0.197
Cl	0.003	0.003	0.002	0.004	0.003	0.005	0.003	0.004	0.006	0.003	0.003	0.002	0.028	0.001
Ba	0.036	0.101	0.090	0.072	0.093	0.101	0.082	0.081	0.050	0.11	0.01	0.07	0.12	0.04
Total	16	16	16	16	16	16	16	16	16	16	16	16	16	16
Mg#	0.67	0.66	0.66	0.67	0.66	0.67	0.67	0.67	0.63	0.61	0.64	0.78	0.66	0.76

Table 1. *Continued.*

Mineral	Phlogopite xenocrysts													
Analysis	1	2	3	4	5	6	7	8	9	10	11	12	13	14
SiO_2	37.72	37.94	37.27	38.02	38.35	37.79	37.81	37.89	37.80	38.34	37.89	36.52	37.14	36.41
TiO_2	4.62	4.52	4.13	4.69	4.50	4.22	4.15	4.58	4.32	4.24	4.46	4.35	4.54	4.63
Al_2O_3	14.62	14.61	14.18	14.70	14.59	14.93	14.62	14.75	14.14	15.01	15.22	15.08	14.52	15.15
FeO	6.19	6.33	8.43	6.65	6.52	7.93	6.20	6.06	6.25	6.61	7.28	9.64	6.26	9.30
MnO	0.09	0.04	0.08	0.03	0.07	0.14	0.10	0.00	0.04	0.05	0.01	0.16	0.00	0.08
MgO	19.61	19.58	16.79	18.62	19.55	19.05	20.11	19.36	19.06	19.89	19.16	18.54	19.38	18.71
CaO	0.09	0.04	0.16	0.16	0.20	0.11	0.20	0.17	0.18	0.19	0.18	0.11	0.16	0.14
Na_2O	0.30	0.31	0.37	0.37	0.37	0.38	0.32	0.38	0.34	0.43	0.42	0.47	0.44	0.53
K_2O	9.02	8.74	8.66	8.54	8.26	8.86	7.84	8.13	8.60	7.67	8.13	8.45	8.74	6.03
Cr_2O_3	1.49	1.51	1.62	1.69	1.01	1.05	1.14	1.27	1.20	0.60	0.51	0.06	1.27	0.00
F	0.53	0.59	0.50	0.53	0.48	0.33	0.63	0.71	0.40	0.56	0.41	0.61	0.59	0.56
Cl	0.02	0.02	0.02	0.00	0.02	0.02	0.03	0.04	0.03	0.03	0.03	0.02	0.01	0.02
BaO	0.00	0.00	0.11	0.02	0.00	0.15	0.00	0.08	0.00	0.04	0.04	0.41	0.15	1.10
Total	94.30	94.33	92.45	94.20	94.09	95.16	93.20	93.42	92.39	93.64	93.92	94.55	93.23	92.78
	Cations based on 22 oxygen atoms													
Si	5.509	5.535	5.615	5.556	5.584	5.506	5.550	5.561	5.611	5.585	5.536	5.421	5.498	5.453
Ti	0.507	0.495	0.468	0.516	0.493	0.463	0.459	0.506	0.482	0.464	0.490	0.486	0.505	0.522
Al	2.517	2.512	2.517	2.531	2.503	2.564	2.529	2.550	2.473	2.577	2.620	2.638	2.534	2.673
Fe^{2+}	0.756	0.772	1.062	0.813	0.793	0.966	0.761	0.743	0.776	0.805	0.889	1.197	0.775	1.164
Mn	0.011	0.005	0.010	0.003	0.008	0.018	0.013	0.000	0.005	0.006	0.002	0.020	0.000	0.010
Mg	4.269	4.258	3.770	4.056	4.244	4.137	4.401	4.235	4.217	4.319	4.172	4.102	4.277	4.177
Ca	0.014	0.006	0.026	0.025	0.031	0.017	0.032	0.027	0.028	0.029	0.028	0.018	0.025	0.022
Na	0.084	0.089	0.107	0.104	0.103	0.107	0.091	0.109	0.099	0.121	0.119	0.136	0.128	0.154
K	1.680	1.626	1.665	1.592	1.534	1.647	1.468	1.522	1.628	1.424	1.515	1.600	1.651	1.153
Cr	0.172	0.174	0.193	0.195	0.116	0.121	0.132	0.147	0.140	0.069	0.059	0.007	0.149	0.000
F	0.244	0.272	0.237	0.243	0.222	0.153	0.291	0.332	0.188	0.258	0.192	0.284	0.275	0.264
Cl	0.005	0.005	0.005	0.001	0.006	0.004	0.007	0.009	0.007	0.007	0.008	0.004	0.003	0.005
Ba	0.000	0.000	0.007	0.001	0.000	0.009	0.000	0.004	0.000	0.002	0.002	0.024	0.009	0.065
Total	16	16	16	16	16	16	16	16	16	16	16	16	16	16
Mg#	0.85	0.85	0.78	0.83	0.84	0.81	0.85	0.85	0.84	0.84	0.82	0.77	0.85	0.78

(*Continued*)

Table 1. *Continued.*

Mineral	Spinel														
Analysis	1	2	3	4	5	6	7	8	9	10	11	12	13	14	15
SiO_2	0.03	0.05	0.08	0.05	0.05	0.03	0.09	0.05	0.08	0.08	0.03	0.02	0.03	0.07	0.08
TiO_2	11.37	12.19	9.99	11.70	11.39	11.08	13.97	13.24	0.10	19.31	12.42	14.11	16.36	13.44	13.72
Al_2O_3	0.03	1.16	0.30	1.70	1.79	2.08	1.74	1.99	0.00	1.28	2.02	1.89	1.30	1.72	2.04
FeO	78.13	76.45	77.62	74.60	74.66	75.24	74.81	74.43	90.82	68.92	75.66	73.38	72.56	74.51	74.27
MnO	1.37	1.40	2.23	2.54	2.84	2.76	2.10	1.99	0.02	1.38	1.88	2.16	2.30	1.96	1.93
MgO	0.00	0.03	0.04	0.05	0.03	0.02	0.13	0.17	0.02	1.86	0.14	0.17	0.13	0.10	0.12
CaO	0.12	0.12	0.70	0.11	0.05	0.05	0.02	0.03	0.15	0.08	0.03	0.03	0.02	0.03	0.02
Cr_2O_3	0.05	0.07	0.05	0.06	0.06	0.07	0.05	0.06	0.05	0.10	0.06	0.06	0.06	0.05	0.05
V_2O_3	0.14	0.10	0.08	0.21	0.16	0.17	0.10	0.22	0.00	0.47	0.20	0.43	0.44	0.14	0.14
Total	91.24	91.57	91.08	91.01	91.03	91.50	93.01	92.19	91.25	93.47	92.44	92.24	93.20	92.02	92.37
	Cations based on 32 oxygen atoms														
Si	0.008	0.016	0.025	0.015	0.015	0.011	0.027	0.014	0.025	0.024	0.008	0.006	0.008	0.021	0.024
Ti	2.721	2.895	2.384	2.786	2.711	2.619	3.262	3.113	0.025	4.456	2.910	3.320	3.831	3.172	3.221
Al	0.013	0.430	0.112	0.633	0.668	0.770	0.636	0.732	0.000	0.462	0.742	0.696	0.477	0.636	0.749
Fe^{3+}	10.480	9.704	11.037	9.695	9.823	9.910	8.748	8.944	15.889	6.439	9.358	8.530	7.721	8.931	8.712
Fe^{2+}	10.319	10.482	9.555	10.061	9.935	9.868	10.670	10.508	7.981	11.245	10.346	10.665	11.164	10.616	10.672
Mn	0.369	0.375	0.598	0.682	0.762	0.736	0.551	0.528	0.005	0.357	0.497	0.571	0.607	0.520	0.511
Mg	0.000	0.015	0.018	0.021	0.012	0.011	0.061	0.080	0.011	0.850	0.065	0.081	0.062	0.048	0.055
Ca	0.041	0.040	0.238	0.037	0.017	0.015	0.007	0.011	0.052	0.028	0.010	0.009	0.006	0.009	0.007
Cr	0.013	0.017	0.012	0.016	0.015	0.017	0.012	0.015	0.012	0.023	0.016	0.014	0.015	0.013	0.013
V	0.035	0.025	0.021	0.054	0.041	0.043	0.026	0.055	0.000	0.117	0.049	0.108	0.109	0.035	0.036
TOTAL	24	24	24	24	24	24	24	24	24	24	24	24	24	24	24
$Fe^{2+}/(Fe^{2+} + Mg)$	1.00	1.00	1.00	1.00	1.00	1.00	0.99	0.99	1.00	0.93	0.99	0.99	0.99	1.00	0.99
$Ti/(Ti + Cr + Al)$	0.99	0.87	0.95	0.81	0.80	0.77	0.83	0.81	0.67	0.90	0.79	0.82	0.89	0.83	0.81

Table 1. *Continued.*

Mineral	Nepheline								
Analysis	1	2	3	4	5	6	7	8	9
SiO_2	43.23	42.57	42.72	42.53	43.15	41.27	42.91	42.53	42.37
Al_2O_3	33.42	34.08	32.98	33.54	33.56	34.29	32.59	31.75	31.88
FeO	0.66	0.58	0.58	0.57	0.29	0.51	0.74	0.71	0.76
MgO	0.00	0.00	0.00	0.00	0.00	0.00	0.00	0.01	0.03
CaO	0.18	0.46	0.00	0.40	0.00	0.00	0.05	0.58	0.50
Na_2O	16.44	14.22	17.03	16.58	16.52	16.87	15.99	16.56	16.36
K_2O	6.58	6.84	6.78	6.79	7.00	7.68	6.77	6.25	6.46
Cr_2O_3	0.00	0.00	0.00	0.00	0.00	0.00	0.00	0.00	0.01
P2O5	0.00	0.00	0.00	0.00	0.00	0.00	0.00	0.00	0.01
BaO	0.00	0.00	0.00	0.00	0.00	0.00	0.00	0.09	0.00
F	0.29	0.09	0.31	0.39	0.02	0.00	0.12	0.21	0.19
Cl	0.00	0.00	0.00	0.00	0.00	0.00	0.00	0.00	0.01
Total	100.79	98.84	100.40	100.80	100.55	100.61	99.16	98.68	98.59
	Cations based on 32 oxygen atoms								
Si	8.313	8.281	8.283	8.216	8.300	8.012	8.377	8.374	8.352
Al	7.573	7.812	7.535	7.635	7.609	7.845	7.499	7.369	7.406
Fe^{2+}	0.106	0.095	0.094	0.092	0.047	0.083	0.120	0.116	0.126
Mg	0.000	0.000	0.000	0.000	0.000	0.000	0.000	0.002	0.008
Ca	0.037	0.095	0.000	0.082	0.000	0.000	0.010	0.123	0.106
Na	6.128	5.363	6.401	6.211	6.161	6.348	6.052	6.323	6.254
K	1.613	1.698	1.676	1.673	1.718	1.901	1.685	1.571	1.626
Cr	0.000	0.000	0.000	0.000	0.000	0.000	0.000	0.000	0.002
P	0.000	0.000	0.000	0.000	0.000	0.000	0.000	0.000	0.002
Ba	0.000	0.000	0.000	0.000	0.000	0.000	0.000	0.007	0.000
F	0.179	0.056	0.192	0.238	0.015	0.000	0.075	0.130	0.121
Cl	0.000	0.000	0.000	0.000	0.000	0.000	0.000	0.000	0.003
Total	24	24	24	24	24	24	24	24	24
Ne	*76.9*	*70.9*	*78.6*	*76.9*	*76.8*	*77.7*	*76.0*	*77.3*	*76.8*
Ks	*20.2*	*22.4*	*20.6*	*20.7*	*21.4*	*21.3*	*21.2*	*19.2*	*20.0*
An	*0.8*	*2.1*	*0.0*	*1.7*	*0.0*	*0.0*	*0.2*	*2.5*	*2.2*
Si	*2.1*	*4.5*	*0.8*	*0.7*	*1.8*	*1.0*	*2.6*	*1.0*	*1.1*

Mineral	Sodalite		
Analysis	1	2	3
SiO_2	37.35	36.55	37.13
Al_2O_3	29.88	31.16	31.09
FeO	0.00	0.19	0.24
MgO	0.00	0.00	0.00
CaO	0.00	0.00	0.00
Na_2O	26.59	26.74	26.54
K_2O	0.00	0.00	0.00
Cr_2O_3	0.00	0.00	0.00
P2O5	0.00	0.00	0.00
BaO	0.00	0.00	0.00
F	0.21	0.00	0.00
Cl	7.23	6.97	6.95
Total	101.27	101.61	101.94

Mineral	Sphene	
Analysis	1	2
SiO_2	29.75	30.05
TiO_2	35.89	35.64
Al_2O_3	1.19	1.35
FeO	1.29	1.44
CaO	27.49	28.43
P_2O_5	0.58	0.64
V_2O_3	0.10	0.41
ZrO_2	0.26	0.39
Total	96.54	98.35

(*Continued*)

Table 1. *Continued.*

Mineral	Feldspar											
Analysis	1	2	3	4	5	6	7	8	9	10	11	12
SiO_2	640.96	63.18	62.53	62.80	64.32	62.08	63.51	64.68	61.21	63.65	63.91	64.33
Al_2O_3	18.23	18.22	17.35	17.85	17.98	17.99	17.26	17.95	19.09	18.52	17.71	18.03
FeO	0.33	0.36	0.24	0.18	0.35	0.32	0.09	0.21	0.35	0.25	0.26	0.36
CaO	0.00	0.00	0.57	0.00	0.00	0.01	0.00	0.00	0.02	0.00	0.00	0.01
Na_2O	2.06	1.61	1.11	0.44	1.89	1.54	0.97	0.70	1.75	1.42	2.08	0.67
K_2O	13.43	14.01	14.90	15.70	13.74	12.75	15.14	14.74	12.01	14.48	13.40	15.54
F	0.00	0.09	0.00	0.00	0.03	0.16	0.03	0.01	0.04	0.08	0.00	0.00
Cl	0.01	0.00	0.02	0.02	0.00	0.00	0.00	−0.05	0.00	0.01	0.00	0.02
BaO	0.46	0.55	0.37	0.25	0.00	2.34	0.00	0.25	3.62	0.00	0.00	0.00
Total	99.48	98.06	97.12	97.26	98.33	97.28	97.03	98.54	98.16	98.43	97.40	98.38
	Cations based on 32 oxygen atoms											
Si	12.016	11.935	11.967	11.977	12.013	11.968	12.080	12.076	11.808	11.917	12.035	12.006
Al	3.974	4.057	3.912	4.012	3.957	4.088	3.870	3.950	4.341	4.086	3.929	3.966
Fe^{2+}	0.051	0.057	0.038	0.029	0.054	0.052	0.014	0.033	0.057	0.039	0.040	0.057
Ca	0.000	0.000	0.116	0.000	0.000	0.001	0.000	0.000	0.003	0.000	0.000	0.003
Na	0.738	0.588	0.413	0.164	0.685	0.577	0.358	0.252	0.653	0.514	0.758	0.242
K	3.168	3.377	3.637	3.819	3.273	3.136	3.674	3.511	2.956	3.460	3.219	3.700
F	0.000	0.057	0.000	0.000	0.019	0.097	0.017	0.003	0.025	0.050	0.000	0.000
Cl	0.002	0.000	0.005	0.006	0.000	0.002	0.000	−0.016	0.000	0.004	0.000	0.006
Ba	0.033	0.041	0.028	0.018	0.000	0.177	0.000	0.018	0.274	0.000	0.000	0.000
Total	20	20	20	20	20	20	20	20	20	20	20	20
An	*0.0*	*0.0*	*2.8*	*0.0*	*0.0*	*0.0*	*0.0*	*0.0*	*0.1*	*0.0*	*0.0*	*0.1*
Ab	*18.9*	*14.8*	*9.9*	*4.1*	*17.3*	*15.5*	*8.9*	*6.7*	*18.1*	*12.9*	*19.1*	*6.1*
Or	*81.1*	*85.2*	*87.3*	*95.9*	*82.7*	*84.4*	*91.1*	*93.3*	*81.8*	*87.1*	*80.9*	*93.8*

n.a., not analysed or means below the EPMA detection limit.

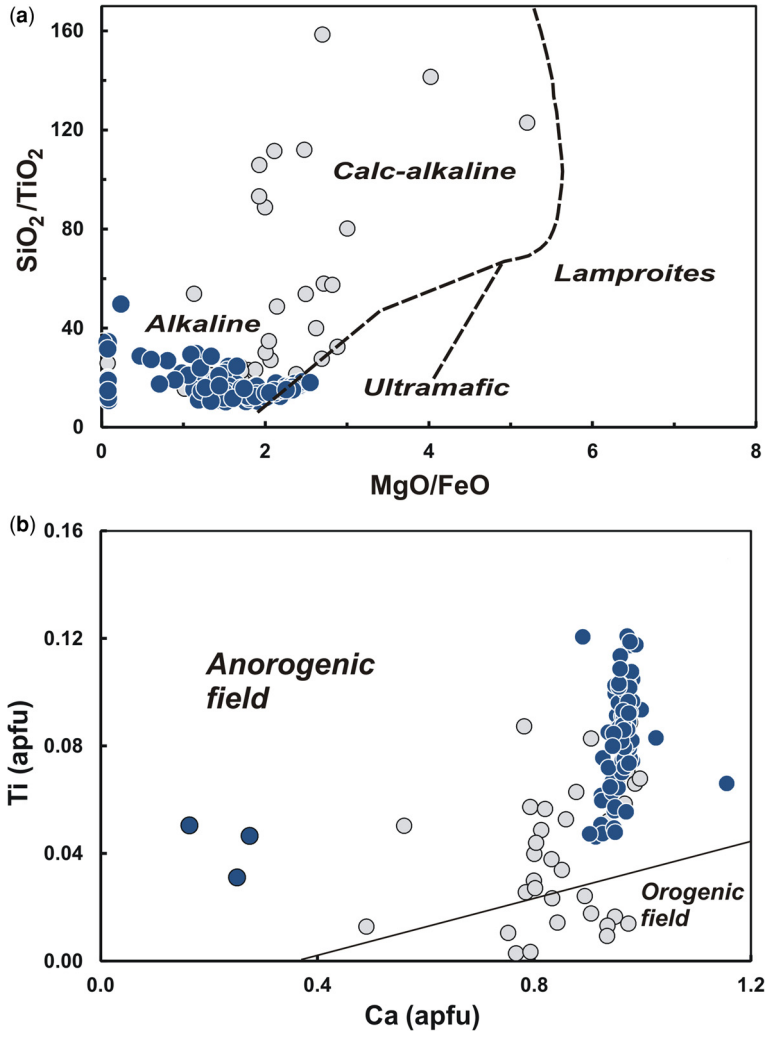

Fig. 4. (**a**) Variation of MgO/FeO v. SiO_2/TiO_2 for clinopyroxenes, different fields are from Rock (1991). All samples show marked affinity to alkaline lamprophyre field. (**b**) Ca (apfu) v. Ti (apfu) tectonic discrimination diagram for clinopyroxenes (after Sun and Bertrad 1991). Grey circles in both the diagrams represent clinopyroxene data from other Deccan lamprophyres. (Data sources: Hari 1998; Chalapathi Rao *et al.* 2012; Sahoo *et al.* 2020.)

Phlogopite. Chemical compositions of most mica crystals display higher amounts of Mg#, FeO_T and TiO_2 and compositionally are phlogopites. These phlogopite grains occur in two parageneses, one as euhedral to subhedral, small-size (usually less than 500 μ) phenocrysts, which are abundant constituents of the groundmass (Figs 2d & 3a) and crystallized from lamprophyre magma. Others occur as large size xenocrysts of usually more than 500 μ in size that show features of deformation and appear to be disintegrated fragments of larger grains.

Core compositions of these two types of phlogopites display wide variations in their major elemental concentrations (e.g. Mg, Fe, Cr and Ba) and Mg# [$=100 \times Mg/(Mg + Fe)$] (Fig. 5). The groundmass phlogopites, which are crystallized from the lamprophyre magma, are characterized by low Mg# (60–78) and Cr_2O_3 (up to 0.34 wt%), and high FeO (8–15 wt%) and BaO (0.19–2 wt%). Phlogopites crystallized from other small-volume, volatile-rich magmas such as kimberlites also show high concentrations of Ba, Ti and low Cr (Giuliani *et al.* 2016; Dongre and Tappe 2019). Xenocrystic phlogopites, on the other hand, are characterized by higher amounts of Mg# (77–85) and Cr_2O_3 (up to 1.7 wt %) and lower FeO (6–9 wt%) and BaO (<1 wt%),

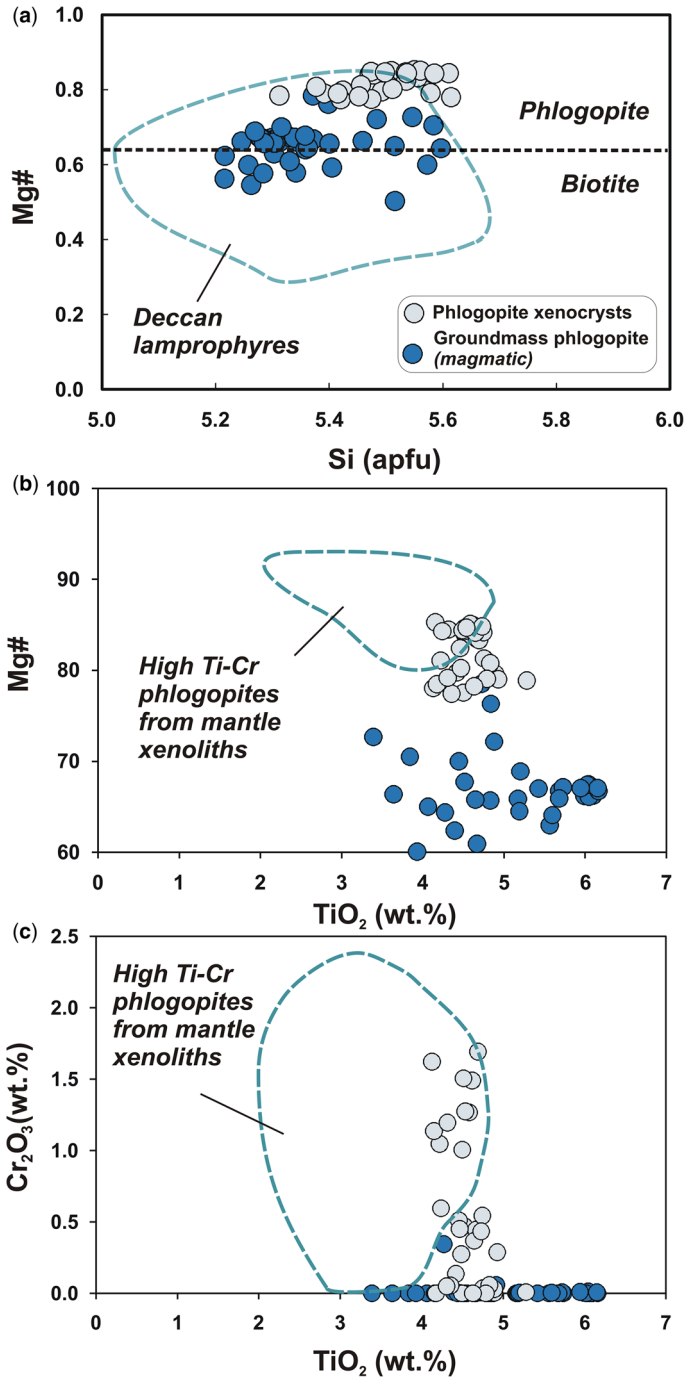

Fig. 5. (**a**) Compositions of mica from SDL samples showing higher Mg# and classified mostly as phlogopites on the Si (apfu) v. $Mg/(Mg + Fe^{2+})$ diagram (Reider *et al.* 1998); note the elevated Mg# in xenocrystic phlogopites that clearly differentiates them from lamprophyric (magmatic) phlogopites. Compositional field of micas from Deccan lamprophyres is from Sahoo *et al.* (2020); (**b**) TiO_2 (wt%) v. Mg# and (**c**) TiO_2 (wt%) v. Cr_2O_3 (wt%) plot for studied phlogopites. Field for high Ti-Cr phlogopites is from Giuliani *et al.* (2016) and Kargin *et al.* (2019). Xenocrystic phlogopites have more affinity to the high Ti-Cr phlogopites from the mantle xenoliths.

and are compositionally similar to the phlogopites from mantle xenoliths (Fig. 5). TiO_2 content in both types of phlogopites varies between 3 and 6 wt%.

Feldspar and nepheline. Feldspars occur only as a groundmass constituent as subhedral to anhedral grains (Fig. 3d, e). They are typically orthoclase in composition (Fig. 6a). However, in Deccan lamprophyres great diversity in feldspar composition is observed, as shown in Figure 6a, which is a characteristic of alkaline lamprophyres.

Feldspathoids are also restricted only to the groundmass, typically present as euhedral crystals (Fig. 3e). Compositionally they are nephelines and sodalites in a few instances. Sodalites show higher Na_2O (*c.* 26 wt%) and Cl^- (*c.* 7 wt%) whereas in nephelines Na_2O varies from 14 to 16 wt%. The presence of nepheline and sodalite confirms the alkaline nature of the studied lamprophyre dyke (Rock 1991). The nepheline compositions are richer than the Morozewicz–Buerger compositions and indicate their higher formation temperatures similar to the nephelines from alkaline and ultramafic lamprophyres (Fig. 6b).

Spinel. Spinels are abundant in the groundmass and are Cr_2O_3 (<0.1 wt%) and MgO (<1.8 wt%) depleted. They are substantially enriched in both $Fe^{2+}/(Fe^{2+} + Mg)$ and $Ti/(Ti + Cr + Al)$ contents and are titanomagnetites in composition (Table 1). They contain high amounts of TiO_2 up to 20 wt% and FeO_T (67–79 wt%). Few grains are pure magnetites with up to 90 wt% FeO_T.

Whole rock geochemistry

Whole-rock major and trace element compositions of the representative samples are provided in Table 2. Bulk rock major element concentrations, particularly SiO_2 (43–44 wt%) demonstrated the silica undersaturation and mafic nature of this rock. In the TAS diagram (Le Bas *et al.* 1986; Fig. 7a) the higher amounts of total alkalis (*c.* 10 wt%) and low SiO_2 are similar to the foidite field of the alkaline series. The presence of nepheline in the groundmass accounts for the higher whole-rock Na_2O content (up to 6.5 wt%) and depicts the alkali-rich nature of the parent magma. Slightly higher amounts of Na_2O than the K_2O (up to 4.5 wt%) in SDL are similar to the other alkaline lamprophyres from the Deccan (Fig. 7b). It shows consistently moderate Mg# values ranging between 43 and 45 (Fig. 7c), that indicate the comparatively evolved nature of its primary magma. Al_2O_3 and Fe_2O_3 show restricted contents of *c.* 16 wt % and *c.* 8 wt%, respectively. It contains high TiO_2, which is essentially more than 2 wt%, showing its alkaline character.

The compatible trace elements like Ni (<20 ppm) and Co (<25 ppm) are very similar to the Chhota Udepur (Ni: 10 to 80 ppm; Co: 17–29 ppm; Chalapathi Rao *et al.* 2012; Pandey *et al.* 2019) and Girnar (Ni: 20 to 70 ppm; Co: <25 ppm; Sahoo *et al.* 2020) lamprophyres, which further support their differentiated nature. However, these compositions are significantly lower than the other Deccan alkaline lamprophyres such as Murud Janjira and Chhaktalao lamprophyres (Hari 1998; Melluso *et al.* 2002; Dessai and Viegas 2010), which show the less evolved and primitive nature of their magmas. All the samples from SDL have very similar chondrite normalized REE and primitive mantle normalized multi-element patterns (Fig. 8a, b). Light rare earth elements (LREE) ($La/Sm_N = 7–8$) are significantly enriched over the heavy rare earth elements (HREE) ($Gd/Lu_N = 2$) resulting in a steep and fractionated pattern. SDL samples have quite identical incompatible element compositions when compared to the other Deccan alkaline lamprophyres and are characterized by prominent positive anomalies at Pb and Zr, small spike at Hf and minor depletion at Ti. SDL samples (including other Deccan lamprophyres) lack Nb and Ta depletions, which are characteristic of calc-alkaline lamprophyres.

$^{40}Ar/^{39}Ar$ dating

The abundance of phlogopites as phenocrysts in studied lamprophyre made it physically possible to separate and analyse this major K-bearing phase. Analysed argon isotope and age data are presented in Supplementary Table 1 following the recommendations given recently by Schaen *et al.* (2021), and $^{40}Ar/^{39}Ar$ age spectra are shown in Figure 9 as well as in Supplementary Figure 3.

$^{40}Ar/^{39}Ar$ ages were obtained on four phlogopite samples from the SDL dyke (Table 3). Out of the four 'plateau' ages, sample Bt_3_1_SDL yielded an integrated $^{40}Ar/^{39}Ar$ age of 68.17 ± 1 Ma (97.8% of the total ^{39}Ar released; Fig. 9), sample Bt_3_3_SDL yielded a 'plateau' age of 65.44 ± 1.5 Ma with 81.17% of the cumulative ^{39}Ar released, sample Bt_4_3_SDL yielded an age of 70.15 ± 1.88 Ma (57.98% of ^{39}Ar) and sample Bt_4_4_SDL yielded an age of 67.54 ± 0.9 Ma (99.0% of ^{39}Ar) (Supplementary Fig. 3). Samples Bt_3_1_SDL (68.17 ± 1 Ma) and Bt_3_3_SDL (65.44 ± 1.5 Ma) delivered the best 'plateau' age patterns (McDougall and Harrison 1999), in five or more consecutive steps with higher amounts of the cumulative ^{39}Ar released. We disregarded the other two ages based on their low ^{39}Ar release and fewer consecutive steps showing consistent results.

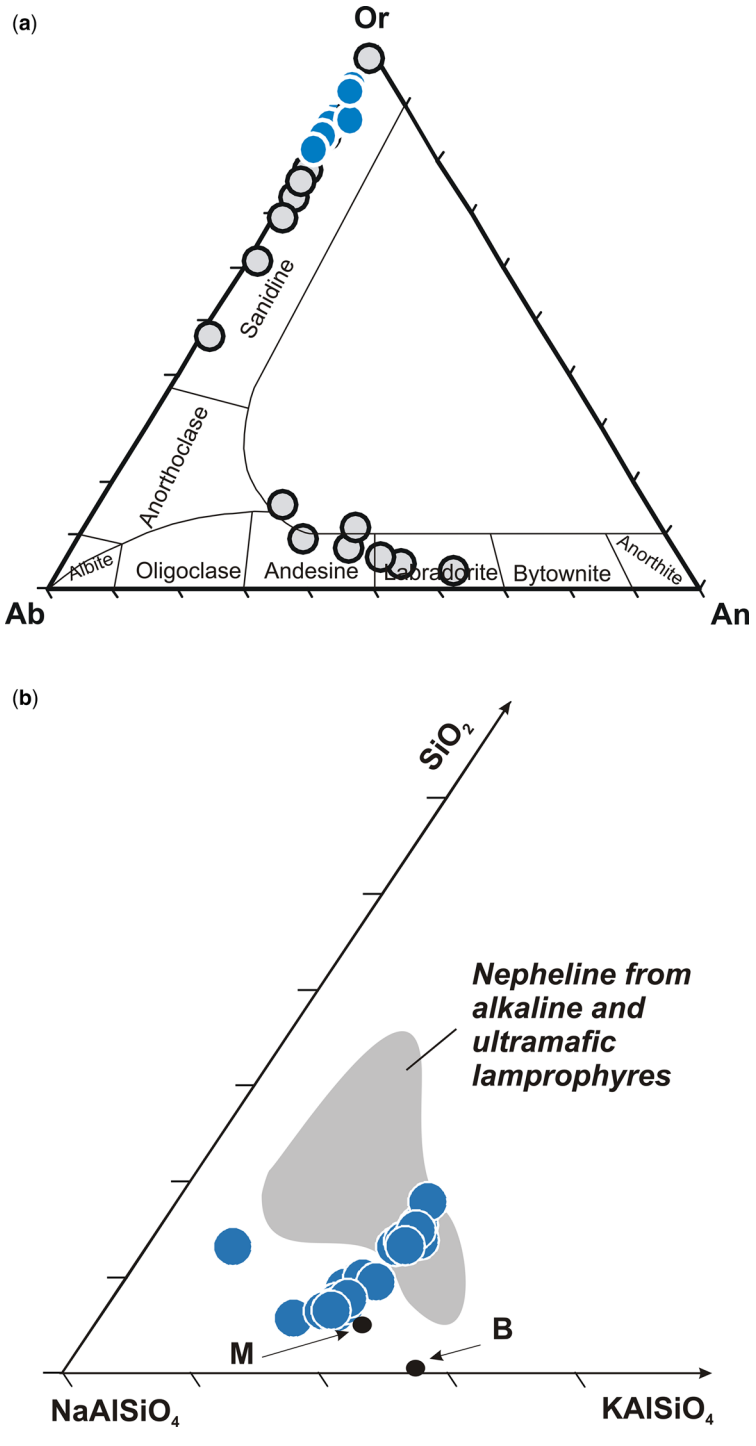

Fig. 6. (**a**) Compositions of feldspar on Ca-Na-K diagram. Grey circles represent Deccan lamprophyres; data compiled from Khan *et al.* (2019). (**b**) Compositions of nepheline plotted in a portion of the nepheline ($NaAlSiO_4$)-Kalsilite ($KAlSiO_4$)-Silica (SiO_2) system; M and B are Morozewicz's and Buerger's ideal nepheline compositions. Field of nepheline from alkaline and ultramafic lamprophyres is from Rock (1991).

Table 2. *Bulk-rock major (in wt%) and trace element (in ppm) compositions of lamprophyre dyke*

Oxide	SDL-1	SDL-2	SDL-3	SDL-4	SDL-5
SiO_2	44.31	43.94	43.83	43.61	43.91
TiO_2	2.36	2.36	2.32	2.47	2.39
Al_2O_3	16.49	16.58	16.59	16.33	16.43
Fe_2O_3	8.52	8.65	8.48	8.66	8.43
MnO	0.22	0.23	0.22	0.23	0.22
MgO	3.37	3.45	3.24	3.54	3.56
CaO	8.42	8.57	8.29	8.82	8.74
Na_2O	5.62	5.73	6.43	6.21	6.46
K_2O	4.47	4.22	4.36	4.13	4.08
P_2O_5	0.45	0.46	0.44	0.48	0.47
Cr_2O_3	0.01	0.00	0.01	0.01	0.01
BaO	0.11	0.10	0.10	0.10	0.11
LOI	5.20	5.30	5.30	5.00	4.70
Total	99.55	99.60	99.61	99.59	99.50
Mg #	43.9	44.1	43.1	44.7	45.6
Trace elements (ppm)					
Rb	125.6	121.3	121.8	116.9	115.6
Cs	2.1	1.9	2.4	2.0	1.9
Sr	1403	1475.3	1451.1	1457.7	1418.7
Ba	1135	1042	1039	1006	1061
Sc	13	13	12	14	14
V	285	287	289	295	279
Co	22.8	24.9	23.0	24.5	24.1
Ni	16.2	16.4	13.4	16.9	16.8
Cu	59.7	76	55.2	63.3	67.8
Zn	100	103	102	85	86
Y	24.2	24.2	23.5	25.8	23.0
Zr	378.3	383.9	372.7	384.5	364.6
Nb	120.3	129.8	125.1	136.7	126.8
Hf	7.2	7.5	7.3	7.3	6.7
Ta	5.1	5	5.1	5	5
W	1.6	1.4	1.2	1.6	1.6
Ga	24.7	25.8	25.2	24.7	24.9
Pb	27.3	36.9	28.3	25.7	27.7
Th	14.3	15.3	13.5	16.6	13.4
U	4.1	3.4	3.6	4.7	3
Rare earth elements (ppm)					
La	89.6	88.4	85.8	95.8	88.1
Ce	142.2	139.1	135.7	148.5	137.5
Pr	14.38	13.69	13.66	15.24	13.3
Nd	48.2	46.5	46.8	51.6	44.8
Sm	7.53	7.22	7.45	7.97	6.92
Eu	2.21	2.18	2.12	2.3	2
Gd	6.44	6.21	6.09	6.42	5.98
Tb	0.84	0.84	0.85	0.87	0.79
Dy	4.64	4.69	4.58	4.75	4.36
Ho	0.84	0.86	0.83	0.87	0.83
Er	2.34	2.25	2.34	2.33	2.2
Tm	0.34	0.32	0.33	0.35	0.31
Yb	2.08	2.16	2.07	2.15	2.09
Lu	0.32	0.32	0.32	0.32	0.31

Mg#, [atomic $Mg/(Mg + Fe^{2+})* 100$].
LOI, loss on ignition.

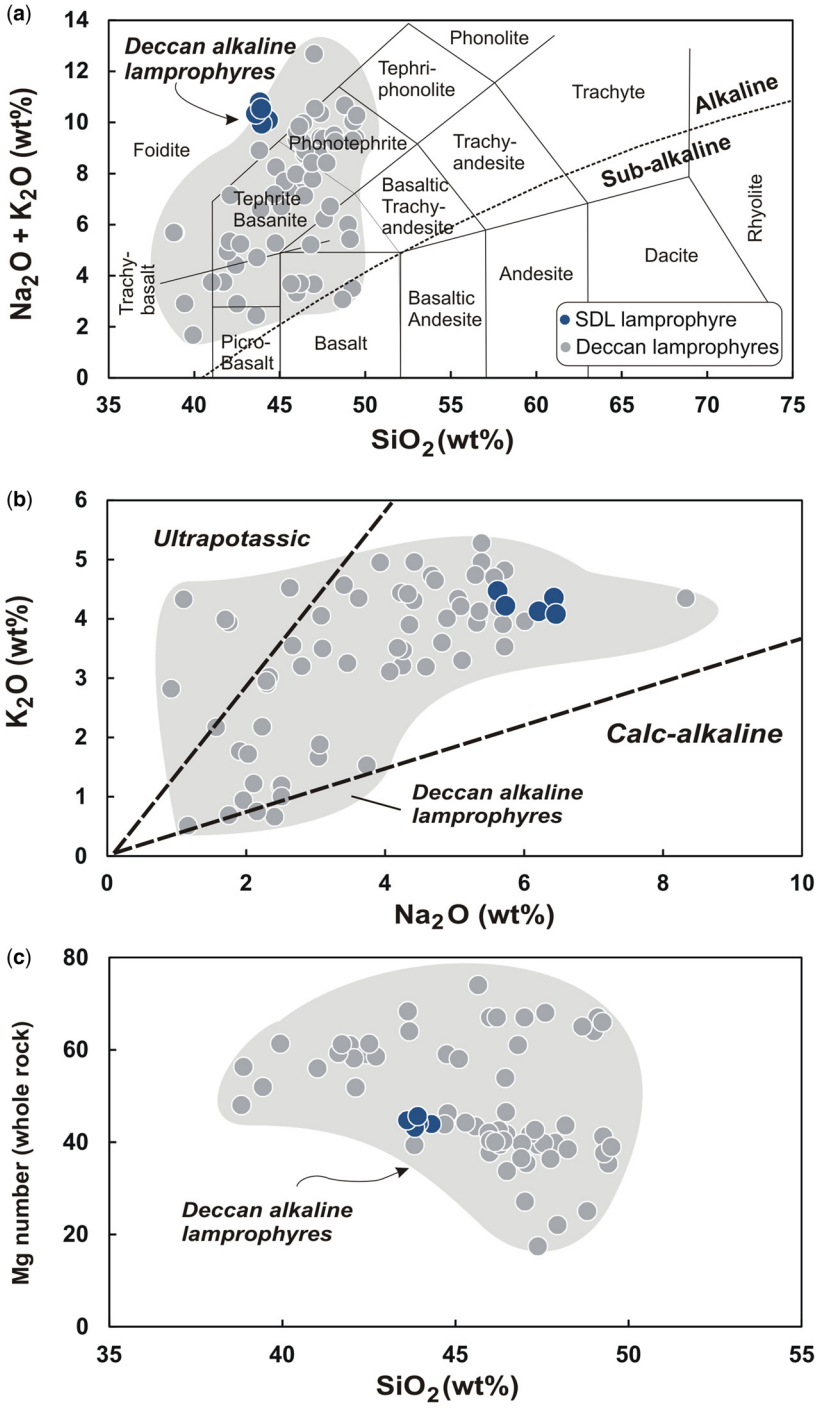

Fig. 7. (**a**) Total-alkali silica (TAS) diagram showing alkaline nature of the Sarnu-Dandali lamprophyre; (**b**) whole-rock compositions displayed on Na_2O (wt%) v. K_2O (wt%) variation diagram, classification fields are from Turner *et al.* (1996); (**c**) SiO_2 vs Mg number (whole-rock) variation for the studied lamprophyre. In all the diagrams, previously reported Deccan alkaline lamprophyres are also plotted in grey circles for comparison. (Data sources: Hari 1998; Dessai and Viegas 2010; Chalapathi Rao *et al.* 2012; Pandey *et al.* 2019; Sahoo *et al.* 2020.)

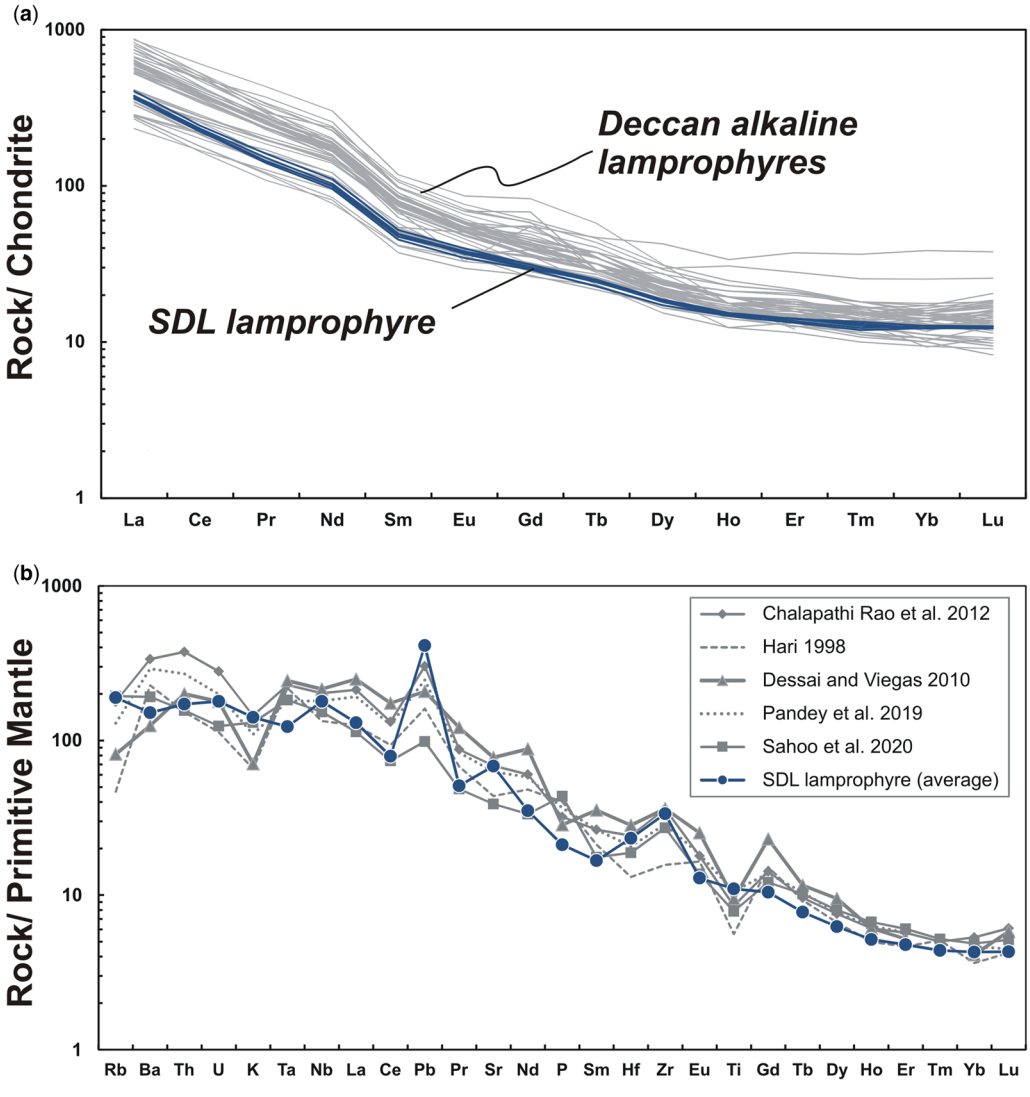

Fig. 8. (**a**) Chondrite normalized REE pattern showing LREE enrichment and HREE depletion; (**b**) primitive-mantle normalized multi-element diagram for the studied lamprophyre. Previously reported Deccan alkaline lamprophyres are also plotted for comparison. Normalization values are from Sun and McDonough (1989).

Palaeomagnetic results

The majority of the samples depicted overlapping or low-angle relations between primary (ChRM) and secondary components during thermal demagnetizations with gradual decay after 300°C. However, after removing the specimens with noisy trajectories in AF demagnetizations, the stable components showed steady demagnetization towards the origin after 25 mT. Table 4 summarizes the stable and reliable directions from the studied lamprophyre dyke and calculated poles. The virtual geomagnetic pole (VGP) obtained fall at 32.31° N and 298.52° E (dp = 10.43; dm = 18.62) matching very well with the Deccan Super Pole (37° N:311° W; at 65.5 Ma).

Discussion

Petrogenesis

The presence of porphyritic-panidiomorphic texture, phenocrysts of clinopyroxene and phlogopite, groundmass feldspar, geochemical alkaline affinity,

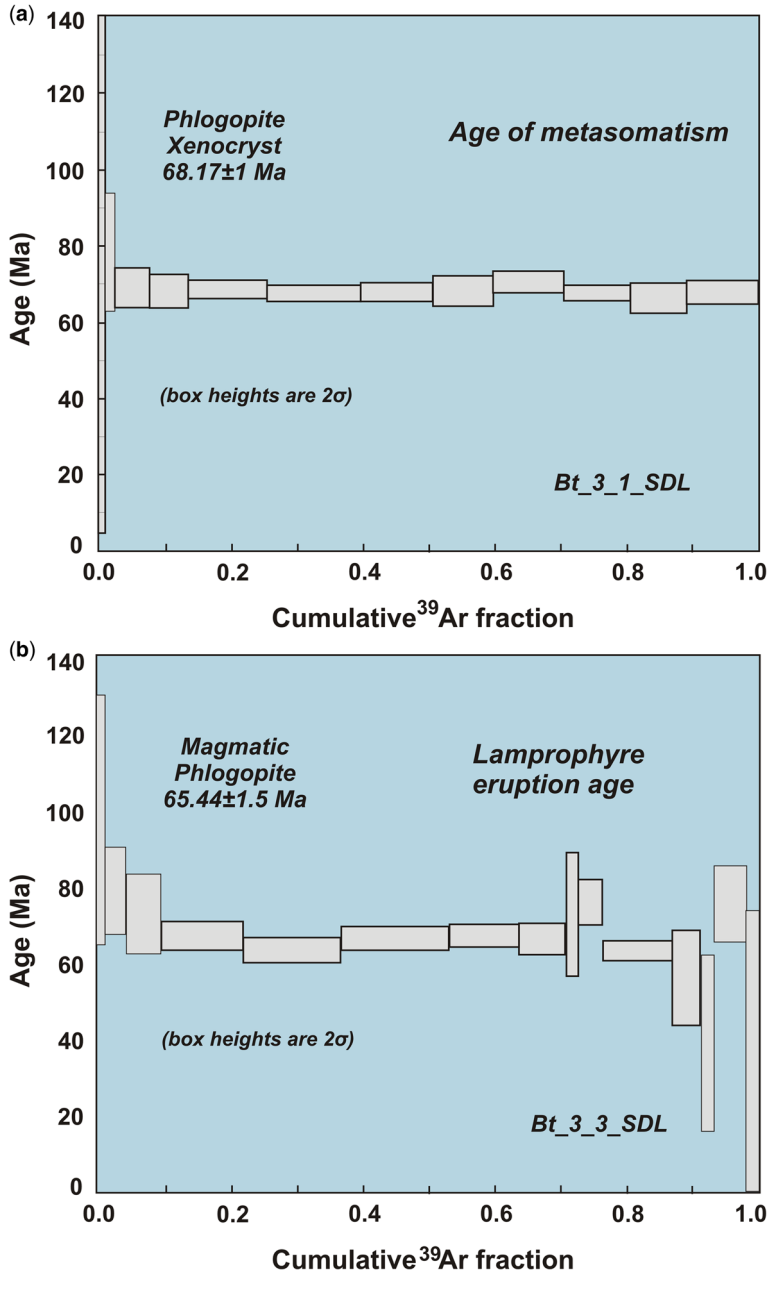

Fig. 9. $^{40}Ar/^{39}Ar$ plateau spectra for phlogopite samples Bt_3_1_SDL (**a**) and Bt_3_3_SDL (**b**) from Sarnu-Dandali lamprophyre dyke.

low content of whole-rock SiO_2 and enrichment in LREE confirms the studied rock to be lamprophyre. Although SDL samples show higher contents of Na_2O and Al_2O_3, the evidence against crustal contamination comes from the lower concentrations of SiO_2 (*c.* 44 wt%). High field strength elements (HFSE) show higher abundances (Nb = 120–137 ppm; Zr = >360 ppm; Pb = >25 ppm; Ce = 136–149 ppm) compared to the continental crust values (Rudnick and Gao 2003). Such high HFSE values negate any significant crustal effects and along with large ion lithophile elements (LILE) enrichment

Table 3. *Summary table indicating $^{40}Ar/^{39}Ar$ plateau age and $^{39}Ar/^{40}Ar - ^{36}Ar/^{40}Ar$ isochron age obtained for Sarnu-Dandali samples*

Sample no.	Mineral	Plateau age (2σ)	$\%^{39}$Ar released	Isochron age (2σ)	Initial $^{40}Ar/^{36}Ar$
Bt_3_1_SDL	Phlogopite	68.17 ± 1 Ma	97.8	69.35 ± 3.8 Ma	287.8 ± 13.9
Bt_3_3_SDL	Phlogopite	65.44 ± 1.5 Ma	81.17	66.31 ± 3.8 Ma	290.8 ± 20.5
Bt_4_3_SDL	Phlogopite	70.15 ± 1.6 Ma	57.98	71.62 ± 1.63 Ma	291.6 ± 5.7
Bt_4_4_SDL	Phlogopite	67.54 ± 0.9 Ma	99.0	68.40 ± 2.41 Ma	292.6 ± 5.7

suggest enrichment of mantle source regions. Enrichment of LREE and very low concentrations of HREE (Lu = 0.32 ppm) also denies significant contamination of felsic crust. LILE are more susceptible to post-magmatic deuteric alteration; however, observed enrichment in LILE elements (Rb, Ba, K and Sr) discounts the post-magmatic alteration effects.

Very minor depletion at Ti does not accompany the Nb anomaly and therefore rules out the role of crustal contamination and convergent margin settings (Pearce 1983). Ti depletion can be explained by the fractionation of Fe-Ti phases during the fractional crystallization process or could be a characteristic of the source magma as observed in all the Deccan lamprophyres.

Figure 10a shows higher amounts of La/Sm for all the Deccan lamprophyres (including SDL samples) corresponding to the ultramafic lamprophyre from Kutch and lower Gd/Lu values compared to ultramafic lamprophyre (Pandey *et al.* 2018*b*). It can be deduced from Figure 10a that relatively higher La/Sm and moderate Gd/Lu may be due to the low amounts of partial melting from the peridotite source. Deccan lamprophyres (including SDL) have relatively shallower source regions than the Kutch UML owing to the lower HREE contents of the latter (Gd/Lu = >5). They also follow the mantle array as depicted by a ratio plot involving HFSEs (Fig. 10b). Their composition is also very similar to the average alkaline lamprophyre (Rock 1991). HFSE concentrations are distinct from the lower and upper crust showing minimum effects of crustal contamination and are more enriched than those of OIB, which necessitates a trace element enriched (metasomatized) source region. Therefore, it appears that metasomatism of mantle source regions of Deccan lamprophyres is triggered due to upwelling alkaline melts or fluids derived from the Réunion mantle plume (e.g. Chalapathi Rao *et al.* 2012). Higher amounts of whole-rock K_2O, LREE enrichment and the presence of phlogopite xenocrysts are indicative of source region enrichment by the metasomatic addition of K_2O and/or H_2O enriched melts/fluids. The K/Rb ratio of SDL samples is >300, which is higher than the average phlogopite (K/Rb = 250) and similar to the average Deccan lamprophyre (K/Rb = 358). The lithospheric mantle source regions of Deccan lamprophyres have strong control of phlogopite (e.g. Pandey *et al.* 2019). Higher Rb/Sr (0.08) and lower Ba/Rb (<10) values also confirm the phlogopite bearing mantle source regions (Fig. 11).

A relatively positive Sr anomaly in the primitive mantle normalized trace element diagram is observed in SDL samples that is absent in other Deccan lamprophyres, but this is not accompanied by Eu anomaly and therefore is not related to the plagioclase fractionation. This is either related to clinopyroxene entrainment or may be a characteristic of source magma. The majority of Deccan alkaline lamprophyres (including SDL) show substantial positive anomalies at Pb and Zr and a relative spike at Hf. Higher Pb and Zr contents are usually found in crustal rocks, therefore their higher abundances along with elevated HREE contents are more likely

Table 4. *Stable and reliable ChRM directions from lamprophyre dyke samples*

Specimen No	Declination	Inclination	MAD	ChRM window	Remarks
16B2-1	323.6	−21.8	8.7	250–450 Oe	AF Demag
16B3-1	314.3	−49.9	8.1	250–450 Oe	AF Demag
16B4-1	302.8	−64.2	4.7	250–450 Oe	AF Demag
16B1-1	302.3	−27.3	12.5	450–580 C	Th Demag
16B1-2	313.9	−17.6	8.4	300–500 C	Th Demag
16B2-1	334.7	−16.8	7.8	350–400 C	Th Demag
16B4-2	334.8	−19.7	7.4	450–580 C	Th Demag
Mean ChRM	319.77	−31.38	A95 = 16.6	k = 14.14	

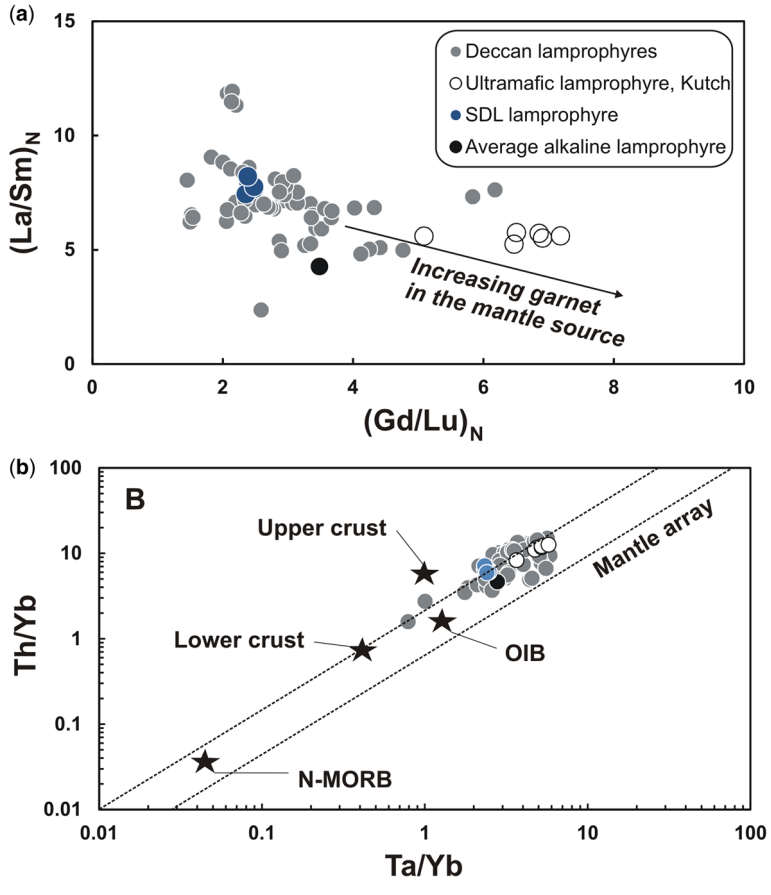

Fig. 10. (**a**) Gd/Lu v. La/Sm (chondrite normalized) and (**b**) Ta/Yb v. Th/Yb (Pearce 1983) variation for the studied lamprophyre dyke plotted with previously reported Deccan alkaline lamprophyres. (Data sources: Hari 1998; Dessai and Viegas 2010; Chalapathi Rao *et al.* 2012; Pandey *et al.* 2018*a*, 2019; Sahoo *et al.* 2020.) Average alkaline lamprophyre is from Rock (1991).

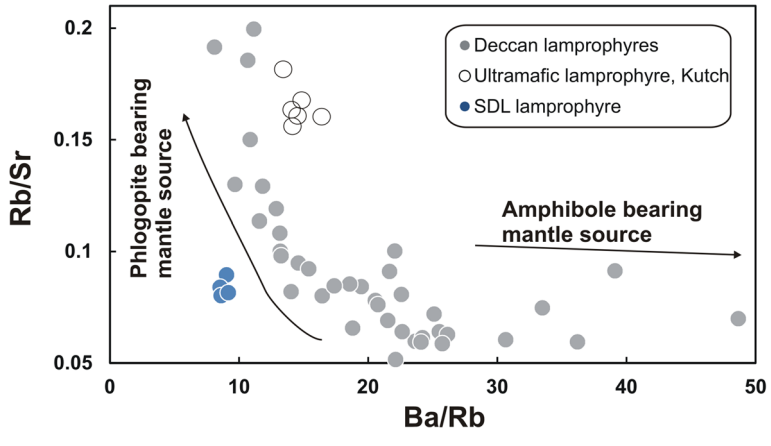

Fig. 11. Ba/Rb v. Rb/Sr variation (after Furman and Graham 1999) for SDL samples and other Deccan alkaline lamprophyres showing dominant control of phlogopite in the mantle source region. Data sources are same as in Figure 10.

due to crustal contamination. However, in SDL samples and in several Deccan lamprophyres, Pb and Zr anomalies are not associated with higher HREE. Assimilation of mafic rocks can elevate the Zr and Hf concentrations on a primitive mantle normalized diagram (Pandey and Chalapathi Rao 2019). A large number of Deccan lamprophyres are intruded in the Deccan tholeiites (as discussed in a later section), which contain the noteworthy positive Pb and Zr anomalies (Vanderkluysen *et al.* 2011; Sheth *et al.* 2019; Patel *et al.* 2020). Therefore, it appears that such anomalies are imprinted by the host basalts or may be source related.

Lamprophyre eruption age

In $^{40}Ar/^{39}Ar$ age dating, in many instances, analysed samples yield 'saddle-shaped' or 'descending staircase' spectra where lower temperature gives an older age than higher temperature, usually attributed to excess argon. Large age ranges may be obtained due to loss or excess of ^{40}Ar during weathering. These factors impose difficulty in identifying proper crystallization age (e.g. Kelley 2002) and for that reason, fresh phlogopite/biotite and plagioclase separates having high K_2O content are preferred for high-precision $^{40}Ar/^{39}Ar$ dating of basaltic and associated alkaline rocks (e.g. Gibson *et al.* 2006; Sprain *et al.* 2019). Recently, Schaen *et al.* (2021) suggested that during incremental heating, plateaus should consist of five or more consecutive steps and at least >50% of the ^{39}Ar released, consecutive plateau steps should not have more ascending or descending ages and distinguishable initial Ar from the atmospheric values. In line with the above, we have considered a release of >70% of the total ^{39}Ar gas in five or more successive steps as a precise age, in this study.

Following the set criteria, only two samples delivered the best 'plateau' ages among four analysed samples. Sample Bt_3_1_SDL gave an age of 68.17 ± 1 Ma, obtained in ten consecutive steps, for 97.8% of the cumulative ^{39}Ar released; and sample Bt_3_3_SDL yielded a 'plateau' age of 65.44 ± 1.5 Ma with 81.17% of the cumulative ^{39}Ar released. Our phlogopite samples do not show any signs of retention of excess radiogenic Ar and yielded similar inverse isochron ages with a specific $^{40}Ar/^{36}Ar$ ratio (*c.* 290) (Table 3). Therefore, we interpret the younger age of *c.* 65.44 ± 1.5 Ma obtained on groundmass phlogopite as an age of the eruption of the lamprophyre dyke. Recently, Sheth *et al.* (2017) also obtained a comparable age of 66.3 ± 0.4 Ma for a mela-nephelinite intrusion from the same Sarnu-Dandali Complex, which supports the younger eruption age of the studied lamprophyre. Consequently, these ages are synchronous to the emplacement of the bulk of Deccan tholeiites. Our palaeomagnetic results yielded a VGP at 32.31° N and 298.52° E, which is concordant with that of the Deccan Super Pole and also supports the younger eruption age. Implications for the older age of *c.* 68 Ma obtained on another sample are discussed later.

Relation of c. 68 Ma phlogopite age and metasomatism of the lithospheric mantle

As mentioned earlier, the presence of xenocrystic phlogopites is a conspicuous feature of the Sarnu-Dandali lamprophyre. Visible clusters of such coarse-grained xenocrystic phlogopites were removed before the sample preparation. However, the possibility of retaining minute broken fragments of the xenocrysts within the lamprophyre groundmass samples cannot be ruled out.

Among the two best 'plateau' ages, sample Bt_3_1_SDL yielded an age of 68.1 ± 1 Ma, which is older than the eruption age of lamprophyre. Since the analysed phlogopite samples do not show any signs of retention of excess radiogenic Ar and display similar inverse isochron ages, we interpreted the obtained older age as a crystallization age of xenocrystic phlogopite.

Phlogopites are generally considered as an indicator of modal metasomatism in the upper mantle within a varied P-T range (O'Reilly and Griffin 2013; Safonov *et al.* 2019). Mantle-derived phlogopites are widely used for estimating the age of melt emplacement or metasomatic events (e.g. Heaman *et al.* 2006; Hopp *et al.* 2008; Larionova *et al.* 2016). In SCLM, phlogopites can crystallize during metasomatism, which transforms garnet peridotite to clinopyroxene-phlogopite rocks because of the pseudomorphing of garnet grains (O'Reilly and Griffin 2013; Kargin *et al.* 2019). They are also present in metasomatic veins and are an important constituent of MARIDs (mica-amphibole-rutile-ilmenite-diopside) and glimmerites (phlogopite-carbonatite) (Gregoire *et al.* 2002). The introduction of metasomatizing fluids and melts during later events is known to be responsible for local refertilization/enrichment of previously strongly depleted mantle and formation of phlogopites within the mantle lithosphere (Pearson *et al.* 2003).

In several studies, it is observed that mantle-derived phlogopite xenocrysts yield older $^{40}Ar/^{39}Ar$ ages than the emplacement age of the host rock (e.g. Phillips and Onstott 1988; Pearson *et al.* 1997; Kelley and Wartho 2000; Johnson and Phillips 2003; Buikin *et al.* 2010; Lehmann *et al.* 2010). Older ages on xenocrystic phlogopite can be obtained either due to (i) incorporation of excess radiogenic ^{40}Ar from a deep fluid source (Phillips 1991; Johnson and Phillips 2003) or (ii) if

phlogopites retain older ages of metasomatism of the lithospheric mantle (Pearson *et al.* 1997; Hopp *et al.* 2008). Phlogopites usually have closure temperature around *c.* 450°C (e.g. Reiners and Brandon 2006). Ar being a highly incompatible element in the major mantle minerals, strongly favours phlogopite in mantle conditions during solid/solid partitioning (Kelley and Wartho 2000). At very high ambient temperatures of the mantle (800–1200°C), the argon system usually behaves as a closed system for phlogopites for several million years (Hopp *et al.* 2008). Hence, in the absence of excess radiogenic ^{40}Ar, the older age of phlogopite reveals the crystallization age of xenocrystic phlogopite and is usually assigned to metasomatism of the lithospheric mantle. In the studied lamprophyre, the high Mg# and Cr concentrations of phlogopite xenocrysts show similar compositions with that of high Ti-Cr phlogopites from kimberlite derived macrocrysts as well as various mantle xenoliths (e.g. polymict breccia, garnet peridotite and clinopyroxene-phlogopite) that occur in global kimberlites (Fig. 5b, c, Giuliani *et al.* 2016; Kargin *et al.* 2019). These xenocrysts are characterized by deformation features (Fig. 2e, f) and may represent disintegrated phlogopite fragments from the metasomatized mantle rocks. Occurrence of phlogopite peridotite xenoliths in the SDL dyke also supports the presence of metasomatized mantle source regions (Supplementary Fig. 1b).

Major tectono-thermal events that influenced the Sarnu-Dandali and Mundwara areas include magmatism related to the break-up of India–Madagascar during timings of the Marion hotspot (at *c.* 90 Ma), and older magmatism of *c.* 102–110 Ma, which is broadly contemporaneous with Rajmahal-Sylhet Traps of eastern India (Pande *et al.* 2017; Sheth *et al.* 2017). These events, which are earlier than the Deccan, must have significantly depleted the local subcratonic lithospheric mantle and modified its composition at Sarnu-Dandali and Mundwara areas. The older age of 68.1 $\pm$ 1 Ma of xenocrystic phlogopite broadly corresponds to the separation of Seychelles–Laxmi Ridge (referred to as Greater Seychelles) and India at *c.* 68.5 Ma, which occurred much before the eruption of voluminous Deccan tholeiites (Bhattacharya and Yatheesh 2015). As a consequence of *c.* 68.5 Ma lithospheric breakup, the local subcratonic lithospheric mantle beneath the Cambay rift and adjacent to it, might have been influenced by fluid or melt migration and undergone metasomatism. Metasomatism was strongly related to the India– Greater Seychelles separation because after interaction with the Marion hotspot at *c.* 90 Ma no other tectono-thermal event was witnessed by the investigated lithospheric mantle/study area until the emplacement of Deccan age alkaline magmatism of lamprophyre and mela-nephelinite.

Absence of pre-Deccan ages in the Sarnu-Dandali and Mundwara complexes

Sarnu-Dandali Alkaline Complex has been considered as pre-Deccan based on a single ^{40}Ar/^{39}Ar age of 68.57 $\pm$ 0.08 Ma analysed from biotite separates from alkali pyroxenite rock (Basu *et al.* 1993) for which petrographic and mineralogical details are not available. As mentioned earlier, Sheth *et al.* (2017) carried out detailed field geological and geochronological investigations in the Sarnu-Dandali area, and obtained ages of 88.9–86.8 Ma for syenite, nephelinite, phonolite and rhyolite, and 66.3 $\pm$ 0.4 Ma age for mela-nephelinite. Along with presently studied lamprophyre age, these ages confirm the presence of the Deccan synchronous age component and older *c.* 90 Ma magmatism related to the Marion hotspot in the Sarnu-Dandali area and non-existence of pre-Deccan magmatism.

Basu *et al.* (1993) also reported a weighted mean plateau age of 68.53 $\pm$ 0.16 Ma (2σ) for biotite separates from alkali olivine gabbro from Toa pluton of the Mundwara Complex. In this study amphibole from mela-gabbro provided saddle-shaped spectra with minimum step ages of *c.* 71 Ma. Rathore *et al.* (1996) obtained ^{40}Ar/^{39}Ar ages between 64 and 75 Ma on varied samples of gabbro, basalts and syenites. But these ages are also characterized by the saddle-shaped spectra that have been considered diagnostic of excess argon content. It is also important to note that biotites from slowly cooled igneous rocks, despite showing well-developed plateau spectra, sometimes show anomalously high ages and need to be interpreted with caution (Foland 1983). In a recent study, Pande *et al.* (2017) provided petrographic and mineral compositional details of the biotites from different mafic rocks of the Mundwara complex. They obtained well-developed ^{40}Ar/^{39}Ar plateau and isochron ages, where primary biotites from mafic rocks (including olivine gabbro from Toa pluton) show 80–84 Ma ages and nepheline syenite show 102–110 Ma whole-rock ages. In this study, the pre-Deccan age component is apparently missing from the Mundwara area too. Recently, Sharma *et al.* (2021), based on Sr-Nd isotopic compositions, suggested plume type asthenospheric derivation corresponding to the Réunion plume for the two lamprophyre dykes from Mundwara and other Deccan lamprophyres. Therefore, these recent studies imply that the Sarnu-Dandali and Mundwara complexes are polychronous, having Deccan and older age components but the pre-Deccan ages are altogether absent. It is highly likely that the biotites/phlogopites showing pre-Deccan ages from the Sarnu-Dandali (and Mundwara as well) are part of a xenocrystic suite showing a crystallization age of *c.* 68.5 Ma, which is related to the metasomatism of the mantle lithosphere.

Absence of pre-Deccan alkaline magmatism related to the Réunion plume

Similar to the Sarnu-Dandali area, extensive geochronological studies recently carried out on the northern Deccan Province did not reveal any pre-Deccan (Maastrichtian age) alkaline magmatism (Parisio *et al.* 2016). However, there are limited occurrences of such rocks reported previously from the northwestern parts of the Indian subcontinent and discussed here. Nevertheless, the availability of high-precision ages for these occurrences is a real-time challenge. A recent study by Sen *et al.* (2016) obtained $^{40}Ar/^{39}Ar$ plateau age of 66.86 $\pm$ 0.16 Ma (with 59% of the total ^{39}Ar released) for hornblende separated from a lamprophyre dyke at Kaladongar area in northern Kutch. However, the sample shows extraneous non-atmospheric argon and an initial apparent age of 90 Ma that decreases to 67 Ma. It, therefore, appears to be younger than the estimated age. Plagioclase separates from Sadara sill from the same Kutch area also yielded older concordant incremental heating plateau ages of 75.81 $\pm$ 0.55 Ma. Although these ages are older than the Deccan, they were considered to be manifestations of the Marion plume magmatism and related to the separation of India and Madagascar (Sen *et al.* 2016).

The only exception to our observation of the absence of pre-Deccan alkaline magmatism is the occurrences of alkaline, mafic-ultramafic magmatism in the Quetta area, south of the Tethyan suture zone (north-western part of the Indian subcontinent). Ultramafic lamprophyre from this area is reported to have a weighted mean $^{40}Ar/^{39}Ar$ plateau age of 69.7 $\pm$ 0.2 Ma yielded from phlogopite and amphibole separates (Kerr *et al.* 2010). From the same area, Mahoney *et al.* (2002) obtained whole-rock $^{40}Ar/^{39}Ar$ ages for two basaltic flow samples from Bibai volcanics, which gave plateau ages of 73.4 $\pm$ 2.0 Ma and 72.0 $\pm$ 2.1 Ma (2σ). However, it was observed that these basalt ages have significantly large errors and suggested that Bibai volcanics and ultramafic lamprophyre sills have similar ages (Kerr *et al.* 2010). These rocks are emplaced in the proximity and south of the Tethyan suture zone and in an entirely different geological setup compared to the cratonic lithosphere where the bulk of Deccan lavas and associated alkaline rocks intruded. According to Collier *et al.* (2008), the extension in the Gop Rift is related to the magmatism of Quetta (Bibai volcanics) and, therefore, a direct link to the Réunion plume seems to be ambiguous. Consequently, pre-Deccan alkaline magmatism (typically older than 66.6 Ma), emplaced during Maastrichtian and directly related to the Réunion mantle plume, is apparently absent in the Indian continental lithosphere.

Alkaline and small-volume, volatile-rich magmatism in the Deccan and significance of their ages

There is a close temporal and spatial link between alkaline and small-volume, volatile-rich magmatism, voluminous LIPs, and mantle plumes (e.g. Bryan and Ernst 2007). The large igneous provinces are also characterized by a short duration (1–5 million years) of the igneous pulse during which a large proportion (>75%) of the total igneous volume mostly get emplaced. Alkaline rocks can be formed due to low degrees of partial melting of mantle owing to the minor thermal effects from impinging or receding mantle plume (e.g. Gibson *et al.* 2006). Deccan-related alkaline, small-volume, volatile-rich rocks are represented mostly by the lamprophyres and carbonatites, and at a few places Group-2 kimberlites, and they are primarily synchronous to the Deccan tholeiites or younger to them (i.e. post-Deccan) (Fig. 12). The lamprophyres and carbonatites show eruption ages between 65.8–65.2 Ma (see Supplementary Table 2) and are mostly emplaced towards the end part, or continued after the main Deccan event of tholeiite volcanism, which is also supported by the field evidence. These alkaline rocks typically intruded the Deccan basalts, as seen in Chhota Udepur (Pandey *et al.* 2019), Girnar (Sahoo *et al.* 2020), Kanesara (Naushad *et al.* 2019) and in Murud-Janjira area (Dessai and Viegas 2010; Hooper *et al.* 2010). An eruption of these rocks at terminal phases and after the main Deccan event, as well as at the peripheral parts of the main Deccan Province implies that they formed in the lithospheric mantle, which has undergone small-fraction melting, due to thermal weakening owing to withdrawing effects of the distant plume. Alternatively, they are just a consequence of lithospheric extension in the pre-existing thin lithosphere near to the rifts (e.g. Cambay, Kutch and Narmada) as well as at the margins of the craton where localized, small-fraction melting of the metasomatized lithospheric mantle has occurred. Emplacements of kimberlite and lamprophyre-carbonatite depend on the composition and evolution of the local subcontinental lithospheric mantle. For instance, in the Bastar craton a long-lived, enriched mantle was preserved, which was suitable for the eruption of Group-2 kimberlites (Chalapathi Rao *et al.* 2011). On the other hand, in the northwestern part of the Indian lithosphere, due to previous interaction with the Marion hotspot in the Late Cretaceous, the long-lived metasomatized mantle was non-existent, since the older enriched mantle lithosphere was destroyed by the plume magmatism, and, therefore, facilitated the formation of only lamprophyres and not kimberlites.

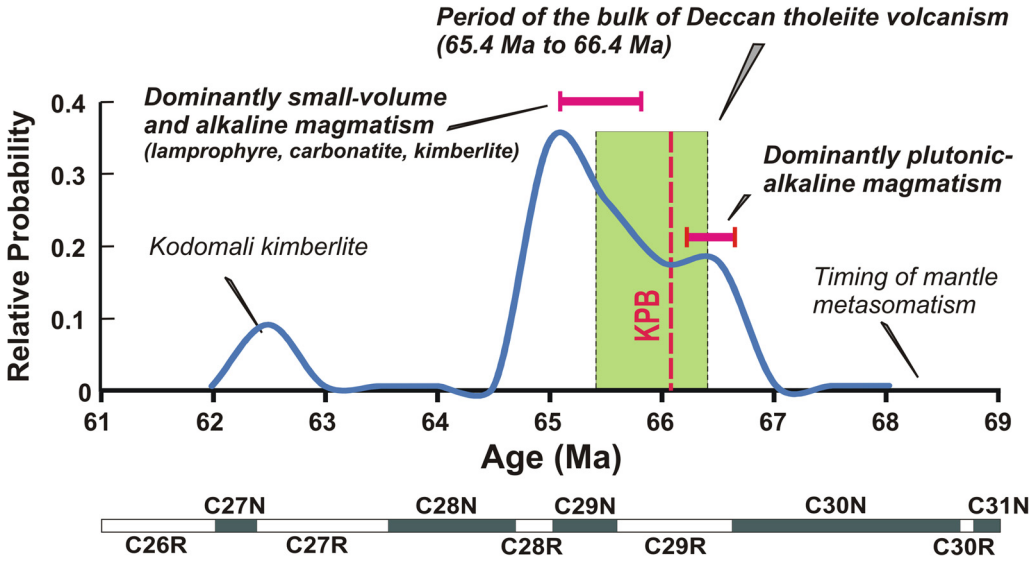

Fig. 12. Age distribution of alkaline and small-volume, volatile rich rocks that are spatially and temporally related to the Deccan LIP ($n = 12$). Only high-precision $^{40}Ar/^{39}Ar$ and U-Pb determinations are utilized. $^{40}Ar/^{39}Ar$ ages on mineral separates that shows >70% ^{39}Ar release in five or more consecutive steps are only considered (data is given in Supplementary Table 2). Green box represents period of voluminous Deccan tholeiite volcanism (66.4–65.4 Ma) and dashed red line represents the Cretaceous–Paleogene Boundary (KPB) (Sprain *et al.* 2019). Geomagnetic polarity is adopted from Parisio *et al.* (2016). In this diagram eruption ages reported by Basu *et al.* (1993) for Sarnu-Dandali and Mundwara complexes and Kerr *et al.* (2010) for Quetta lamprophyres are excluded and explanations are given in the text.

Plutonic alkaline and volatile-rich magmatism mostly occurred during the initial phases and started *c.* 0.2 million years before the main Deccan event just before the Cretaceous–Paleogene Boundary (KPB) (Fig. 12). Plutonic alkaline intrusives of nepheline syenites and alkali gabbros must have formed due to the initial impact of the Réunion plume and associated lithospheric extension. Alkaline intrusions predating the main episode of tholeiitic magmatism have been known from the Ferrar Province of Antarctica that is linked to the Bouvet mantle plume (Riley *et al.* 2003), from the Tarim LIP of China (Zhang *et al.* 2013) and from Parana-Etendeka LIP of Brazil where it is related to the initial impact of the Tristan plume (Gibson *et al.* 2006). The 'older' (>67 Ma) alkaline rocks of Maastrichtian age, predating flood basalt eruptions of the Deccan, are either absent or yet not recognized from the Indian subcontinent or buried by the thick pile of tholeiitic lava flows.

Lehmann *et al.* (2010) reported a younger $^{206}Pb/^{238}U$ perovskite date of 62.3 ± 0.8 Ma for a Group 2 kimberlite at Kodomali in the Bastar craton, which was also confirmed by the $^{40}Ar/^{39}Ar$ geochronology that yielded a weighted mean plateau age of 62.1 ± 1.4 Ma. The small-volume, volatile-rich magmatism of Kodomali kimberlite erupted *c.* 2 million years after the hiatus of similar magmatism, and after the emplacement of the majority of lamprophyres and carbonatites (Fig. 12). The age of Kodomali intrusions overlaps with the Early Paleocene break-up of Greater Seychelles into the Seychelles Plateau and the Laxmi Ridge at *c.* 62.5 Ma (Bhattacharya and Yatheesh 2015). It indicates that the Kodomali intrusions are related to the post-Deccan rifting event associated with the separation of the Seychelles Plateau and the Laxmi Ridge, and a direct causal link with the Réunion hotspot appears untenable.

Conclusions

(1) A lamprophyre dyke intruded in syenites and associated with carbonatites from the Sarnu-Dandali Alkaline Igneous Complex is studied here in detail. Mineralogically, the dyke is rich in phlogopite (magmatic and xenocrystic) and clinopyroxene, exhibits a typical panidiomorphic texture and is geochemically similar to other lamprophyres reported previously from the Deccan LIP. Based on mineral and whole-rock geochemical (major and trace elements) compositions it is classified as an

alkaline lamprophyre similar to the other Deccan alkaline lamprophyres. Trace element compositions show small amounts of partial melting and magma derivation from OIB-type enriched (metasomatized) mantle source regions with more involvement of phlogopite.

(2) Our $^{40}Ar/^{39}Ar$ dating of groundmass phlogopite shows an eruption age of 65.44 ± 1.5 Ma, which is broadly similar with the age of 66.3 ± 0.4 Ma obtained recently for a mela-nephelinite intrusion from the Sarnu-Dandali Complex (Sheth *et al.* 2017). Our new geochronological data supported by palaeomagnetic studies confirm the presence of Deccan synchronous alkaline magmatism in the Sarnu-Dandali. Carbonatite intrusions, which are associated with lamprophyre dyke, may essentially be of similar age as well based on their similar field settings.

(3) Our $^{40}Ar/^{39}Ar$ age of 68.17 ± 1 Ma yielded by the xenocrystic phlogopite is almost analogous to the $^{40}Ar/^{39}Ar$ age of 68.5 Ma reported previously from Sarnu-Dandali. The present study reveals that the pre-Deccan ages of *c.* 68–69 Ma, yielded by the phlogopites in the Sarnu-Dandali area, in fact, reflect the timing of metasomatism of the lithospheric mantle that occurred during the separation of the Greater Seychelles from India at *c.* 68.5 Ma. Therefore, absence of pre-Deccan alkaline magmatism related to the Réunion plume does not support the concept of the time-related migration of volcanism in the Deccan LIP on the Indian subcontinent.

(4) The absence of the Réunion plume related pre-Deccan alkaline rocks in the Deccan LIP also supports the short duration of alkaline as well as small-volume, volatile-rich magmatism, which occurred between 67–65 Ma and did not span more than *c.* 2 million years on the Indian subcontinent.

(5) The available high-precision geochronological dataset on lamprophyres, carbonatites and kimberlites shows their eruptions between 65.2 to 66.6 Ma with a post-Deccan peak. The ages and the field settings imply that these rocks formed at a distance from the main volcanic centre or plume head where small-volume magmas generated due to lower amounts of partial melting owing to the minor thermal effects from the withdrawing or distant Réunion plume.

(6) Interestingly, our appraisal of available high-precision ages for alkaline rocks of the Deccan shows the emplacement of dominantly plutonic alkaline magmatism just before the Cretaceous–Paleogene Boundary (KPB) and during the early phase of the main Deccan event. Such emplacements of the volatile-rich alkaline rocks appear to be responsible for the degassing of higher levels of climate-modifying magmatic volatiles (such as CO_2) in the atmosphere before KPB. However, this preliminary model awaits further testing by geochemical means to know the exact amounts of volatile release by these alkaline rocks.

Acknowledgements We are sincerely grateful to Jan Kramers for his help in the $^{40}Ar/^{39}Ar$ analyses. This study benefited from the critical comments by four anonymous reviewers and efficient editorial handling by Lukáš Krmíček and N. V. Chalapathi Rao. AD is grateful to Hetu Sheth and S. K. Bhushan for discussions about the geology of the Sarnu-Dandali complex.

Author contributions **AD**: conceptualization (lead), investigation (lead), project administration (equal), writing – original draft (lead); **PSD**: investigation (equal), methodology (supporting), writing – review & editing (equal); **PZ**: data curation (equal), investigation (supporting), software (supporting); **SJS**: data curation (supporting), resources (equal), validation (supporting); **GB**: data curation (supporting), resources (supporting), validation (supporting); **DCM**: data curation (supporting), resources (supporting), writing – review & editing (supporting); **SKP**: data curation (supporting), resources (supporting), validation (supporting); **AK**: data curation (supporting), resources (supporting); **LJ**: data curation (supporting), software (supporting).

Funding The field work part of this study was supported by the Savitribai Phule Pune University through the DRS grant. We thank Ministry of Earth Sciences for financial support through project no. MoES/PO (Seismo)/8(15)/2018. Aaheri Karmakar thanks DST-SERB for awarding JRF (Project P07/569 of BHU).

Data availability All data generated or analyzed during this study are included in this published article (and its supplementary information files).

References

Basu, A.B., Renne, P.R., DasGupta, D.K., Teichmann, F. and Poreda, R. 1993. Early and late alkali igneous pulses and a high-3He plume origin for the Deccan flood basalts. *Science (New York, N Y)*, **261**, 902–906, https://doi.org/10.1126/science.261.5123.902

Bhattacharya, G.C. and Yatheesh, V. 2015. Plate-tectonic evolution of the deep ocean basins adjoining the western continental margin of India – a proposed model for the early opening scenario. *In*: Mukherjee, S. (ed.) *Petroleum Geoscience: Indian Contexts*. Springer, 1–61.

Bhushan, S.K. 2015. Geology of the Kamthai rare earth deposit. *Journal of the Geological Society of India*, **85**, 537–546, https://doi.org/10.1007/s12594-015-0247-y

Bhushan, S.K. and Kumar, A. 2013. First carbonatite hosted REE deposit from India. *Journal of the Geological Society of India*, **81**, 41–60, https://doi.org/10.1007/s12594-013-0005-y

Bladon, A.J., Burley, S.D., Clarke, S.M. and Beaumont, H. 2015. Geology and regional significance of the Sarnoo Hills, eastern rift margin of the Barmer Basin, NW India. *Basin Research*, **27**, 636–655, https://doi.org/10.1111/bre.12093

Bryan, S. and Ernst, R. 2007. Revised definition of large igneous province (LIP). *Earth Science Reviews*, **86**, 175–202, https://doi.org/10.1016/j.earscirev.2007.08.008

Buikin, A.I., Trieloff, M., Korochantseva, E.V., Hopp, J., Kaliwoda, M., Meyer, H.-P. and Altherr, R. 2010. Distribution of mantle and atmospheric argon in mantle xenoliths from the Western Arabian Peninsula: constraints on timing and composition of metasomatizing agents in the lithospheric mantle. *Journal of Petrology*, **51**, 2547–2570, https://doi.org/10.1093/petrology/egq073

Chalapathi Rao, N.V., Lehmann, B., Mainkar, D. and Belyatsky, B. 2011. Petrogenesis of the end-Cretaceous diamondiferous Behradih orangeite pipe: implication for mantle plume–lithosphere interaction in the Bastar craton, Central India. *Contributions to Mineralogy and Petrology*, **161**, 721–742, https://doi.org/10.1007/s00410-010-0559-2

Chalapathi Rao, N.V., Dharma Rao, C.V. and Das, S. 2012. Petrogenesis of lamprophyres from Chhota Udepur area, Narmada rift zone and its relation to Deccan magmatism. *Journal of Asian Earth Sciences*, **45**, 24–39, https://doi.org/10.1016/j.jseaes.2011.09.009

Chandrasekaran, V., Srivastva, R.K. and Chawade, M.P. 1990. Geochemistry of the alkaline rocks of Sarnu Dandali area, district Barmer, Rajasthan, India. *Journal of the Geological Society of India*, **36**, 365–382.

Chenet, A.L., Quidelleur, X., Fluteau, F., Courtillot, V. and Bajpai, S. 2007. ^{40}K–^{40}Ar dating of the Main Deccan large igneous province: further evidence of KTB age and short duration. *Earth and Planetary Science Letters*, **263**, 1–15, https://doi.org/10.1016/j.epsl.2007.07.011

Collier, J.S., Sansom, V., Ishizuka, O., Taylor, R.N., Minshull, T.A. and Whitmarsh, R.B. 2008. Age of Seychelles-India break-up. *Earth and Planetary Science Letters*, **272**, 264–277, https://doi.org/10.1016/j.epsl.2008.04.045

Conrad, J.E., Hein, J.R., Chaudhuri, A.K., Patranabis-Deb, S., Mukhopadhyay, J., Deb, G.K. and Beukes, N.J. 2011. Constraints on the development of Proterozoic basins in central India from Ar-40/Ar-39 analysis of authigenic glauconitic minerals. *Geological Society of America Bulletin*, **123**, 158–167, https://doi.org/10.1130/B30083.1

Dessai, A.G. and Viegas, A. 2010. Petrogenesis of alkaline rocks from Murud-Janjira, in the Deccan Traps, Western India. *Mineralogy and Petrology*, **98**, 297–311, https://doi.org/10.1007/s00710-009-0105-y

Dhote, P.S. 2015. *Petrogenesis of lamprophyres and carbonatites from north-west Indian Deccan volcanic province*. Geological Survey of India Report.

Dolson, J., Burley, S.D. *et al*. 2015. The discovery of the Barmer Basin, Rajasthan, India, and its petroleum geology. *American Association of Petroleum Geologists Bulletin*, **99**, 433–465, https://doi.org/10.1306/10021414045

Dongre, A., Viljoen, K.S. and Rathod, A. 2017. Mineralogy and geochemistry of picro-dolerite dykes from the central Deccan Traps flood basaltic province, India, and their geodynamic significance. *Mineralogy and Petrology*, **112**, 267–277, https://doi.org/10.1007/s00710-017-0539-6

Dongre, A.N. and Tappe, S. 2019. Kimberlite and Carbonatite dykes within the Premier diatreme root (Cullinan diamond Mine, South Africa): New insights to mineralogical-genetic classifications and magma CO_2 degassing. *Lithos*, **338–339**, 155–173, https://doi.org/10.1016/j.lithos.2019.04.020

Foland, K.A. 1983. $^{40}Ar/^{39}Ar$ incremental heating plateaus for biotites with excess argon. *Isotope Geoscience*, **1**, 3–21.

Furman, T. and Graham, D. 1999. Erosion of lithospheric mantle beneath the East African Rift system: geochemical evidence from the Kivu volcanic province. *Lithos*, **48**, 237–262, https://doi.org/10.1016/S0024-4937(99)00031-6

Gibson, S.A., Thompson, R.N. and Day, J.A. 2006. Timescales and mechanisms of plume- lithosphere interactions: $^{40}Ar/^{39}Ar$ geochronology and geochemistry of alkaline igneous rocks from the Parana-Etendeka large igneous province. *Earth and Planetary Science Letters*, **251**, 1–17, https://doi.org/10.1016/j.epsl.2006.08.004

Giuliani, A., Phillips, D., Kamenetsky, V.S. and Goemann, K. 2016. Constraints on kimberlite ascent mechanisms revealed by phlogopite compositions in kimberlites and mantle xenoliths. *Lithos*, **240–243**, 189–201, https://doi.org/10.1016/j.lithos.2015.11.013

Gregoire, M., Bell, D.R. and Le Roex, A.P. 2002. Trace element geochemistry of phlogopite-rich mafic mantle xenoliths: their classification and their relationship to phlogopite-bearing peridotites and kimberlites revisited. *Contributions to Mineralogy and Petrology*, **142**, 603–625, https://doi.org/10.1007/s00410-001-0315-8

Hari, K.R. 1998. Mineralogical and petrochemical studies of the lamprophyres around Chhaktalao area, Madhya Pradesh. *Journal of the Geological Society of India*, **51**, 21–30.

Heaman, L., Creaser, R., Cookenboo, H. and Chacko, T. 2006. Multi-stage modification of the northern slave mantle lithosphere: evidence from zircon- and diamond bearing eclogite xenoliths entrained in Jericho kimberlite, Canada. *Journal of Petrology*, **47**, 821–858, https://doi.org/10.1093/petrology/egi097

Hopp, J., Trieloff, M. *et al*. 2008. $^{40}Ar/^{39}Ar$-ages of phlogopite in mantle xenoliths from South African kimberlites: evidence for metasomatic mantle impregnation during the Kibaran orogenic cycle. *Lithos*, **106**, 351–364, https://doi.org/10.1016/j.lithos.2008.09.001

Hooper, P., Widdowson, M. and Kelley, S. 2010. Tectonic setting and timing of the final Deccan flood basalt eruptions. *Geology*, **38**, 839–842, https://doi.org/10.1130/G31072.1

Johnson, L. and Phillips, D. 2003. $^{40}Ar/^{39}Ar$ dating of mantle metasomatism: a noble approach or all hot air? *8th International Kimberlite Conference, Victoria, Long Abstract*.

Kale, V.S., Dole, G., Shandilya, P. and Pande, K. 2019. Stratigraphy and correlations in Deccan volcanic province, India: Quo vadis?. *Geological Society of America Bulletin*, **132**, 588–607, https://doi.org/10.1130/B35018.1

Kargin, A.V., Sazonova, L.V. *et al*. 2019. Phlogopite in mantle xenoliths and kimberlite from the Grib pipe, Arkhangelsk province, Russia: evidence for multi-stage mantle metasomatism and origin of phlogopite in kimberlite. *Geoscience Frontiers*, **10**, 1941–1959, https://doi.org/10.1016/j.gsf.2018.12.006

Kelley, S.P. 2002. Excess argon in K–Ar and Ar–Ar geochronology. *Chemical Geology*, **188**, 1–22, https://doi.org/10.1016/S0009-2541(02)00064-5

Kelley, S.P. and Wartho, J.-A. 2000. Rapid ascent and the significance of Ar-Ar ages in xenolith phlogopites. *Science (New York, N Y)*, **289**, 609–611, https://doi.org/10.1126/science.289.5479.609

Kerr, A.C., Khan, M., Mahoney, J.J., Nicholson, K.N. and Hall, C.M. 2010. Late Cretaceous alkaline sills of the south Tethyan suture zone, Pakistan: initial melts of the Réunion hotspot. *Lithos*, **117**, 161–171, https://doi.org/10.1016/j.lithos.2010.02.010

Khan, S., Dongre, A., Viljoen, F., Li, Q.-L. and Le Roux, P. 2019. Petrogenesis of lamprophyres synchronous to kimberlites from the Wajrakarur kimberlite field: implications for contrasting lithospheric mantle sources and geodynamic evolution of the eastern Dharwar Craton of southern India. *Geological Journal*, **54**, 2994–3016, https://doi.org/10.1130/B35018.1

Kossert, K. and Günther, E. 2004, LSC measurements of the half-life of ^{40}K. *Applied Radiation and Isotopes*, **60**, 459–464, https://doi.org/10.1016/j.apradiso.2003.11.059

Larionova, Y.O., Sazonova, L.V., Lebedeva, N.M., Nosova, A.A., Tretyachenko, V.V. and Kargin, A.V. 2016. Kimberlite age in the Arkhangelsk Province, Russia: isotopic geochronologic Rb-Sr and 40Ar/39Ar and mineralogical data on phlogopite. *Petrology*, **24**, 562–593, https://doi.org/10.1134/S0869591116040020

Le Bas, M.J., Le Maitre, R.W., Streckeisen, A. and Zanettin, B. 1986. A chemical classification of volcanic rocks based on the total alkali-silica diagram. *Journal of Petrology*, **27**, 745–750, https://doi.org/10.1093/petrology/27.3.745

Lehmann, B., Burgess, R., Frei, D., Belyatski, B., Mainkar, D., Chalapathi Rao, N.V. and Heaman, L.M. 2010. Diamondiferous kimberlites in central India synchronous with Deccan flood basalts. *Earth and Planetary Science Letters*, **290**, 142–149, https://doi.org/10.1016/j.epsl.2009.12.014

Mahoney, J.J., Duncan, R.A., Khan, W. and Gnos, E. 2002. Cretaceous volcanic rocks of the South Tethyan suture zone, Pakistan: implications for the Réunion hotspot and Deccan traps. *Earth and Planetary Science Letters*, **203**, 295–310, https://doi.org/10.1016/S0012-821X(02)00840-3

McDougall, I. and Harrison, T.M. 1999. *Geochronology and Thermochronology by the 40Ar/39Ar Method*. Oxford University Press.

Melluso, L., Sethna, S.F., D'Antonio, M., Javeri, P. and Bennio, L. 2002. Geochemistry and petrogenesis of sodic and potassic mafic alkaline rocks in the Deccan Volcanic Province, Mumbai area (India). *Mineralogy and Petrology*, **74**, 323–342, https://doi.org/10.1007/s007100200009

Narsimhan, C.L., Arora, B.R. and Patil, S.K. 2019. Rock magnetic and palaeomagnetic studies on the alkaline complexes of western Rajasthan, India. *Journal of Earth System Sciences*, **128**, 1–11, https://doi.org/10.1007/s12040-019-1249-8

Naushad, M., Dongre, A., Behera, J.R., Murthy, P.V.R. and Chakra, M. 2019. Mineralogy of a new occurrence of lamprophyre dyke from the Saurashtra Peninsula of Gujarat, Northwest Deccan Trap, India. *Journal of the Geological Society of India*, **93**, 629–637, https://doi.org/10.1007/s12594-019-1241-6

O'Reilly, S.Y. and Griffin, W.L. 2013. Mantle metasomatism. *In*: Harlov, D.E. and Håkon, A. (eds) *Metasomatism and the Chemical Transformation of Rock SE – 8*. Springer, Berlin, 471–533.

Pande, K. 2002. Age and duration of the Deccan Traps, India: a review of radiometric and paleomagnetic constraints. *Proceedings of the Indian Academy of Science (Earth and Planetary Science)*, **111**, 115–123, https://doi.org/10.1007/BF02981139

Pande, K., Cucciniello, C. *et al*. 2017. Polychronous (Early Cretaceous to Palaeogene) emplacement of the Mundwara alkaline complex, Rajasthan, India: ^{40}Ar/^{39}Ar geochronology, petrochemistry and geodynamics. *International Journal of Earth Sciences*, **106**, 1487–1504, https://doi.org/10.1007/s00531-016-1362-8

Pandey, A. and Chalapathi Rao, N.V. 2019. Coupled assimilation and fractional crystallization (AFC) and mantle plume source(s) contribution in the generation of Paleoproterozoic mafic dykes of the eastern Dharwar Craton, southern India. *Journal Geological Society of India*, **93**, 157–162, https://doi.org/10.1007/s12594-019-1144-6

Pandey, R., Chalapathi Rao, N.V., Pandit, D., Sahoo, S. and Dhote, P. 2018*a*. Imprints of modal metasomatism in the post-Deccan subcontinental lithospheric mantle: petrological evidence from an ultramafic xenolith in an Eocene lamprophyre, NW India. *Geological Society, London, Special Publications*, **463**, 117–136, https://doi.org/10.1144/SP463.6

Pandey, R., Chalapathi Rao, N.V., Dhote, P., Pandit, D., Choudhary, A.K., Sahoo, S. and Lehmann, B. 2018*b*. Rift-associated ultramafic lamprophyre (damtjernite) from the middle part of the lower cretaceous (125 Ma) succession of Kutch, north western India: tectonomagmatic implications. *Geoscience Frontiers*, **9**, 1883–1902, https://doi.org/10.1016/j.gsf.2017.10.013

Pandey, R., Pandey, A. *et al*. 2019. Petrogenesis of end-Cretaceous/Early Eocene lamprophyres from the Deccan Large Igneous Province: constraints on plume lithosphere interaction and the post-Deccan lithosphere-asthenosphere boundary (LAB) beneath NW India. *Lithos*, **346–347**, 105–139, https://doi.org/10.1016/j.lithos.2019.07.006

Parisio, L., Jourdan, F., Marzoli, A., Melluso, L., Sethna, S.F. and Bellieni, G. 2016. ^{40}Ar/^{39}Ar ages of alkaline and tholeiitic rocks from the northern Deccan Traps: implications for magmatic processes and the K–Pg boundary. *Journal of the Geological Society of London*, **73**, 679–688, https://doi.org/10.1144/jgs2015-133

Patel, V., Sheth, H. *et al*. 2020. Geochemistry of Deccan tholeiite flows and dykes of Elephanta Island: insights into the stratigraphy and structure of the Panvel flexure zone, western Indian rifted margin. *Geosciences*, **10**, https://doi.org/10.3390/geosciences10040118

Pearce, J.A. 1983. Role of the sub-continental lithosphere in magma genesisat active continental margins. *In*: Hawkesworth, C.J. and Norry, M.J. (eds) *Continental Basalts and Mantle Xenoliths*. Shiva Press, Nantwich, UK.

Pearson, D.G., Kelley, S.P., Pokhilenko, N.P. and Boyd, F.R. 1997. Laser 40Ar/39Ar dating of phlogopites from southern African and Siberian kimberlites and their xenoliths: constraints on eruption ages, melt degassing and mantle volatile compositions. *Russian Journal of Geology and Geophysics*, **38**, 106–117.

Pearson, D.G., Canil, D. and Shirey, S.B. 2003. Mantle samples included in volcanic rocks: xenoliths and diamonds. *In*: Carlson, R.W. (ed.), The mantle and core. *Treatise on geochemistry*. Elsevier, Amsterdam, pp. 171–275.

Phillips, D. 1991. Argon isotope and halogen chemistry of phlogopite from South African kimberlites: a combined step-heating, laser probe, electron microprobe and TEM study. *Chemical Geology*, **87**, 71–98.

Phillips, D. and Onstott, T.C. 1988. Argon isotopic zoning in mantle phlogopites. *Geology*, **16**, 542–546, https://doi.org/10.1130/0091-7613(1988)016<0542:AIZIMP>2.3.CO;2

Rathore, S.S., Venkatesan, T.R. and Srivastava, R.K. 1996. Mundwara alkali igneous complex, Rajasthan, India: chronology and Sr isotope characteristics. *Journal of the Geological Society of India*, **48**, 517–528.

Reider, M., Cavazzini, D. *et al*. 1998. Nomenclature of micas. *Canadian Mineralogist*, **36**, 905–912.

Reiners, P.W. and Brandon, M.T. 2006. Using thermochronology to understand orogenic erosion. *Annual Reviews of Earth and Planetary Science*, **34**, 219–266, https://doi.org/10.1146/annurev.earth.34.031405.125202

Renne, P.R., Swisher, C.C, Deino, A.L., Karner, D.B., Owens, T.L. and DePaolo, D.J. 1998. Intercalibration of standards, absolute ages and uncertainties in $^{40}Ar/^{39}Ar$ dating. *Chemical Geology*, **145**, 117–152, https://doi.org/10.1016/S0009-2541(97)00159-9

Renne, P.R., Mundil, R., Balco, G., Min, K. and Ludwig, K. 2010. Joint determination of ^{40}K decay constants and $^{40}Ar^*/^{40}K$ for the Fish Canyon sanidine standard, and improved accuracy for $^{40}Ar/^{39}Ar$ geochronology. *Geochimca et Cosmochimica Acta*, **74**, 5349–5367, https://doi.org/10.1016/j.gca.2010.06.017

Renne, P.R., Sprain, C.J., Richards, M.A., Self, S., Vanderkluysen, L. and Pande, K. 2015. State shift in deccan volcanism at the cretaceous-Paleogene boundary, possibly induced by impact. *Science (New York, N Y)*, **350**, 76–78, https://doi.org/10.1126/science.aac7549

Riley, T.R., Leat, P.T., Storey, B.C., Parkinson, I. and Millar, I. 2003. Ultramafic lamprophyres of the Ferrar large igneous province: evidence for a HIMU mantle component. *Lithos*, **66**, 1–2, https://doi.org/10.1016/S0024-4937(02)00213-X

Rock, N.M.S. 1991. *Lamprophyres*. Blackie and Sons Ltd., Glasgow.

Rudnick, R.L. and Gao, S. 2003. Composition of the continental crust. *In*: Rudnick, R.L. (ed.) *The Crust*, Holland, H.D. and Turekian, K.K. (eds) Treatise on Geochemistry. Elsevier-Pergamon, Oxford, **3**, 1–64.

Safonov, O., Butvina, V. and Limanov, E. 2019. Phlogopite-forming reactions as indicators of metasomatism in the lithospheric mantle. *Minerals*, **9**, https://doi.org/10.3390/min9110685

Sahoo, S., Chalapathi Rao, N.V., Monie, P., Belyatsky, B., Dhote, P. and Lehmann, B. 2020. Petro-geochemistry, Sr-Nd isotopes and $^{40}Ar/^{39}Ar$ ages of fractionated alkaline lamprophyres from the Mount Girnar igneous complex (NW India): insights into the timing of magmatism and the lithospheric mantle beneath the Deccan Large Igneous Province. *Lithos*, **374–375**, 105712, https://doi.org/10.1016/j.lithos.2020.105712

Schaen, A.J., Jicha, B.R. and Hodges, K.V. and others. 2021. Interpreting and reporting $^{40}Ar/^{39}Ar$ geochronologic data. *GSA Bulletin*, **133**, 461–487, https://doi.org/10.1130/B35560.1

Schoene, B., Samperton, K.M. *et al*. 2015. U-Pb geochronology of the Deccan traps and relation to the end cretaceous mass extinction. *Science (New York, N Y)*, **347**, 182–184, https://doi.org/10.1126/science.aaa0118

Sen, A., Pande, H., Hegner, E., Sharma, K.K., Dayal, A.M., Sheth, H.C. and Mistry, H. 2012. Deccan volcanism in Rajasthan: ^{40}Ar–^{39}Ar geochronology and geochemistry of the Tavidar volcanic suite. *Journal of Asian Earth Science*, **59**, 127–140, https://doi.org/10.1016/j.jseaes.2012.07.021

Sen, G., Hames, W.E., Paul, D.K., Biswas, S.K., Ray, A. and Sen, I.S. 2016. Pre-Deccan and Deccan magmatism in Kutch, India: implications of the new $^{40}Ar/^{39}Ar$ ages of intrusions. *Geological Society of India Special Publication*, **6**, 211–222, https://doi.org/10.17491/cgsi/2016/105422

Sharma, A., Sahoo, S., Chalapathi Rao, N.V., Belyatsky, B., Dhote, P. and Lehmann, B. 2021. Petrology and Nd-Sr isotopic composition of alkaline lamprophyres from the Early to Late Cretaceous Mundwara alkaline complex, NW India: evidence of crystal fractionation, accumulation and corrosion in a complex magma chamber plumbing system. *Geological Society, London, Special Publications*, **513**, https://doi.org/10.1144/SP513-2020-175

Sheth, H.C., Pande, K., Vijayan, A., Sharma, K.K. and Cucciniello, C. 2017. Recurrent early cretaceous, Indo Madagascar (89–86 Ma) and Deccan Trap (66 Ma) alkaline magmatism in the Sarnu-Dandali complex, Rajasthan: $^{40}Ar/^{39}Ar$ age evidence and geodynamic significance. *Lithos*, **284–285**, 512–524, https://doi.org/10.1016/j.lithos.2017.05.005

Sheth, H., Vanderkluysen, L., Demonterova, E.I., Ivanov, A.V. and Savatenkov, V.M. 2019. Geochemistry and $^{40}Ar/^{39}Ar$ geochronology of the Nandurbar-Dhule mafic dyke swarm: Dyke-sill-flow correlations and stratigraphic development across the Deccan flood basalt province. *Geological Journal*, **54**, 157–176, https://doi.org/10.1002/gj.3167

Sprain, J., Renne, P.R., Vanderkluysen, L., Pande, K., Self, S. and Mittal, T. 2019. The eruptive tempo of Deccan volcanism in relation to the Cretaceous-Paleogene boundary. *Science (New York, N Y)*, **363**, 866–870, https://doi.org/10.1126/science.aav1446

Sun, C.M. and Bertrad, J. 1991. Geochemistry of clinopyroxenes in plutonic and volcanic sequences from the Yanbian Proterozoic ophiolites (Sichuan Province, China): petrogenetic and geotectonic implications. *Schweiz Mineralogy Petrology*, **71**, 243–259.

Sun, S.S. and McDonough, W.F. 1989. Chemical and isotopic systematics of oceanic basalts: implications for mantle composition and processes. *Geological Society, London, Special Publications*, **42**, 313–345, https://doi.org/10.1144/GSL.SP.1989.042.01.19

Sun, J., Liu, C.Z. *et al*. 2014. Repeated kimberlite magnetism beneath Yakutia and its relationship to Siberian flood volcanism: insights from *in situ* U–Pb and Sr–Nd perovskite isotope analysis. *Earth and Planetary Science Letters*, **404**, 283–295, https://doi.org/10.1016/j.epsl.2014.07.039

Turner, S., Arnaud, N., Liu, J., Rogers, N., Hawkesworth, C., Harris, N. and Deng, W. 1996. Post-collision, shoshonitic volcanism on the Tibetan plateau: implications for convective thinning of the lithosphere and the source of ocean island basalts. *Journal of Petrology*, **37**, 45–71, https://doi.org/10.1093/petrology/37.1.45

Vanderkluysen, L., Mahoney, J.J., Hooper, P.R., Sheth, H.C. and Ray, R. 2011. The feeder system of the Deccan Traps (India): insights from dyke geochemistry. *Journal of Petrology*, **52**, 315–343, https://doi.org/10.1093/petrology/egq082

Vijayan, A., Sheth, H. and Sharma, K.K. 2016. Tectonic significance of dykes in the Sarnu-Dandali alkaline complex, Rajasthan, northwestern Deccan Traps. *Geoscience Frontiers*, **7**, 783–791, https://doi.org/10.1016/j.gsf.2015.09.004

Zhang, D.Y., Zhang, Z.C., Santosh, M., Cheng, Z.G., Huang, H. and Kang, J.L. 2013. Perovskite and baddeleyite from kimberlitic intrusions in the Tarim Large Igneous Province: signal of the onset of an end-Carboniferous mantle plume. *Earth and Planetary Science Letters*, **361**, 238–248, https://doi.org/10.1016/j.epsl.2012.10.034